國 立 台 灣 大 學 物 理 學 研 究 所

碩士論文

利用時域有限差分法於可調式液晶摻雜2維光子晶體雷射之理論分析

Theoretical Analysis on the Liquid Crystal Infiltrated Tunable 2D Photonic Crystal Laser using Finite-Difference Time-Domain Method

指導教授：趙治宇 教授

研究生：徐明均 (Suh, Myoung Gyun)

中華民國 九十五年 一月

To my family

Contents

Abstract

In recent years, with growing interests to Photonic Crystals (PhCs) and their applications, many researchers have studied PhCs. 2-Dimensional PhC laser is one of the interesting research topics due to its strong light confinement in a small wavelength-scale volume.

Liquid Crystal (LC) infiltrated 2D PhC laser has also been investigated for the laser wavelength tuning, yet its theoretical study seems insufficient. Thus, in this research, we developed 3D Finite-Difference Time-Domain (FDTD) program which can simulate the light propagation in LCs, and analyzed the characteristics of LC infiltrated 2D PhC laser.

In several characteristic PhC structures, the lasing wavelength shift of a single mode, the degeneracy splitting, the lasing mode change and the quality factor (Q-factor) change are found as the arrangement of LCs changes. Moreover, by properly designing the defect, we can expect the intrinsic polarization of the lasing mode.

Acknowledgments

This thesis would not have come into without the help and support of many people. First, I would like to thank my advisor, Professor C. Y. Chao, for supporting my research. I also acknowledge the helpful advice and assistance of S. H. Sia for the experimental steps of this research. My interaction with the other colleagues in Taiwan has been one of the most memorable of my life.

I would also like to thank Professors C. H. Kuan and Y. P. Chiou of the Department of Electrical Engineering in National Taiwan University, and Professor H. L. Liu of the Department of Physics in National Taiwan Normal University, for serving on my thesis committee.

I am also deeply indebted to Professor Y. H. Lee of Korea Advanced Institute of Science and Technology (KAIST) for leading me into the field of Photonic Crystals and for the valuable advices on my career.

I wish to express special thanks to Hui Chen, for her seemingly endless patience and love. I also thanks to her family members, for their support during my stay in Taiwan.

Finally, I must thank to my family for their devoted love.

Chapter 1.

Introduction

Since the concept of the photonic crystal (PhC) [1] has originated, many researchers have studied its characteristics and interest in PhCs has steadily grown in recent years as discovering a lot of applications, such as waveguides [2], optical filters [3], compact lasers [4,5], and quantum information processing [6,7].

The electrical tuning of photonic band gap (PBG) using liquid crystals (LCs) is one of the important topics in PhC research and this specific field has been studied both theoretically and experimentally [8-11].

In this chapter, we will introduce the concept of the LC infiltrated tunable 2D PhC laser [10,11]. For this purpose, we will briefly review the basics of PhCs, 2D PhC lasers and LCs in advance.

1.1. Photonic Crystal and 2D Photonic Crystal Laser

1.1.1. Photonic Crystal

The idea of photonic crystals (PhCs) was born in 1986 by Eli Yablonovitch while he was working at Bell Communications Research in New Jersey. The first PhC structures made by Yablonovitch which is called “Yablonovite” was milli-meter size. Since then, many researchers have studied PhCs both theoretically and experimentally.

In recent years, by the development of submicron fabrication technology, we could make PhCs of submicron lattice constant and PhCs become essential to many optics

fields.

Like all other crystals, PhCs are structures of regularly repeating elements. However, the elements in PhCs are dielectric materials, while those in conventional crystals are atoms or molecules [Table 1.1]. Because of this periodicity of PhCs and multiple Bragg reflection effect, “photonic band gap (PBG)”, which is an anology of electronic band gap in solid state physics, appears in the PhC structures [12]. In Figure 1.2, we can see the photonic band structure of a certain PhC structure.

Table 1.1 Conventional crystals vs. Photonic crystals [12]

	Conventional crystals	**Photonic crystals**
Master equation	Schrödinger equation	Maxwell equation
Periodicity	The potential: $V(r) = V(r+R)$	The dielectric: $\varepsilon(r) = \varepsilon(r+R)$
Natural lenth scale	Usually exist	Not exist (scalable)
Interaction between normal modes	Exist (electron-electron repulsive interactions)	Not exist (In the linear regime)
Band above the gap	Conduction band	Air band
Band below the gap	Valence band	Dielectric band
Defect	Donor atoms pull states from the conduction band into the gap; acceptor atoms pull states from the valence band into the gap	Dielectric defects pull states from the air band into the gap; air defects pull states from the dielectric band into the gap
Applications	Electrical devices	Optical devices

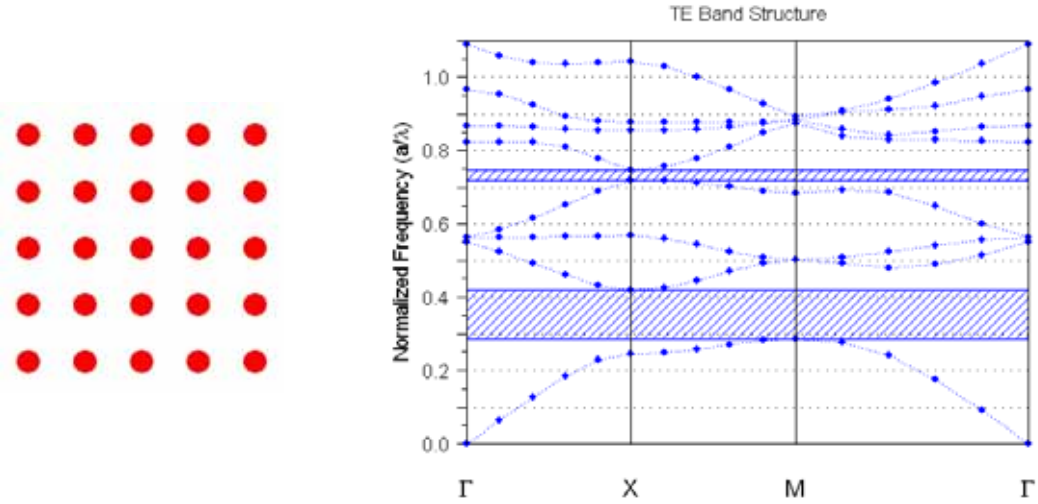

Figure 1.1 2D PhC structure and its photonic band structure

Since lights with the wavelength in the PBG can not propagate in the PhC stuructures, we can control the flow of light using this property of PhCs. Thus, PhCs are suitable structures for making waveguides [2], optical filters [3], compact lasers [4,5], and quantum information processing [6,7].

1.1.2. 2D photonic crystal laser

Owing to the easy fabrication with its strong light confinement in a small volume (wavelength scale), two-dimensional photonic crystal laser (2D PhC laser) is one of the popular topics among the PhC research fields.

The concept of 2D PhC laser is simple and can be easily understood in Figure 1.2. In this figure, the light propagating in-plane direction with certain range of wavelength is confined in the defect of 2D slab because of PBG effect. Moreover, the total internal reflection (TIR) in the slab/air interfaces confines the light in the slab material. Therefore, the light generated by the quantum well slab material is confined in the suitably designed PhC defect and the resonant mode occurs.

In the 2D PhC laser, there are some critical parameters, such as the dielectric index of the slab material, the lattice constant of the PhC structure, the air hole radius, and the shape of the defect. As these parameters are changed, the PBG structure, the resonant mode (lasing mode), and the quality factor (Q factor) also change [13,14]. Thus, the structure need to be well-designed for specific purposes.

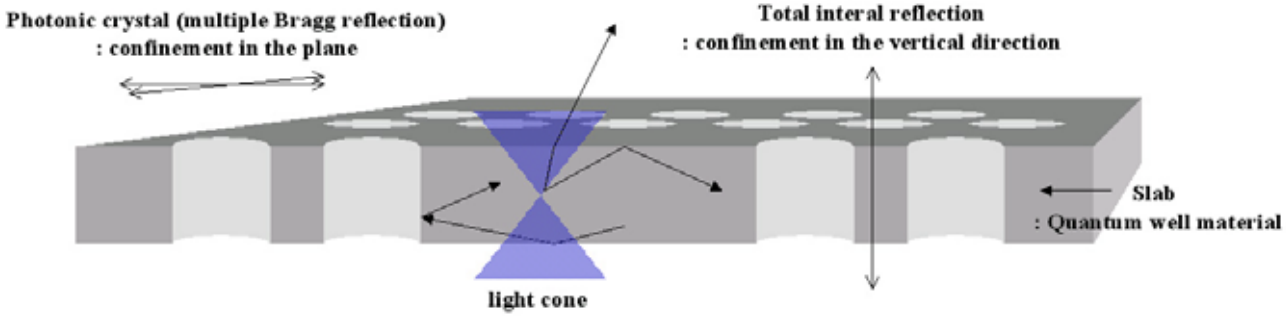

Figure 1.2 The principle of the 2D PhC laser and the basic free-standing structure.

1.2. Liquid Crystal

Liquid crystal (LC) is a state of matter that is intermediate between the crystalline solid and the amorphous liquid. This intermediate state was first observed in 1888 in cholesteryl benzoate, a crystalline solid, and thousand of LC materials are known nowadays [15].

Generally speaking, there are two types of LCs ; thermotropic LCs, which is formed by the temperature change, and lyotropic LCs, which is formed by the concentration change within a solvent [16]. Here, we will only focus on the thermotropic LCs.

There are three phases of thermotropic LCs, known as the smectic phase, the nematic phase, and the cholesteric phase, which are illustrated in Figure 1.3. For the sake of clarity, we assume that the liquid crystals are made of rodlike molecules [15].

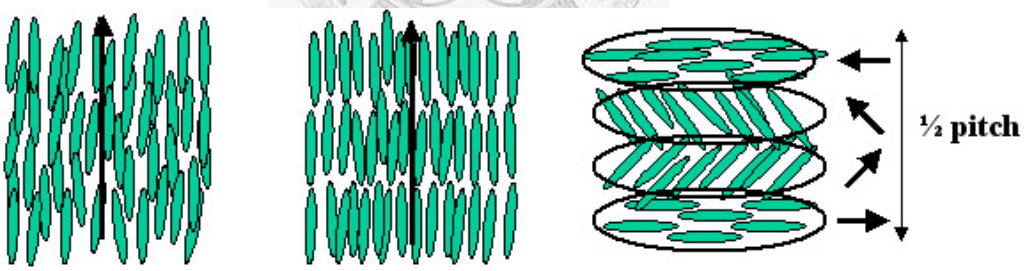

(a) (b) (c)

Figure 1.3 The phases of thermotropic LC. (a) nematic phase (b) smectic phase (c) cholesteric phase

Nematic phase has only a long range orientational order of the molecular axes. Smectic phase has one dimensional translational order as well as orientational order. Cholesteric phase which is also a nematic type of LCs appears when the LC molecules

are chiral, and the spontaneous twist about a helical axis normal to the LC director (The definition of LC director is shown in Figure 1.4) can be seen in this phase [15].

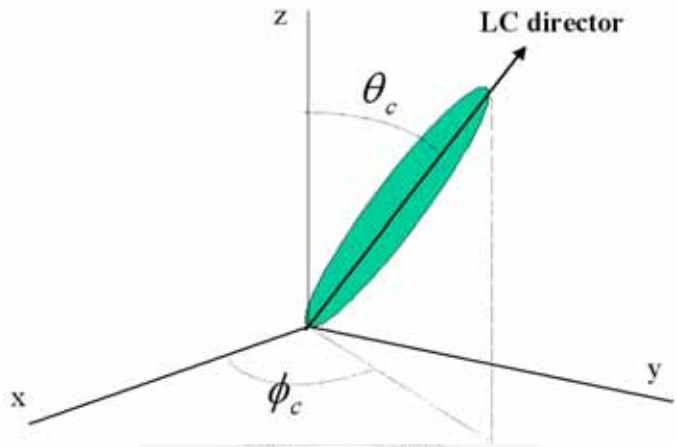

Figure 1.4 The definition of LC director

Generally, LCs arise under certain conditions in organic substances having sharply anisotropic molecules, that is, highly elongated (rodlike) molecules or flat (disklike) molecules. Due to this anisotropic molecular structure, LCs have several characteristics such as dielectic and optical anisotropy [15].

Under proper treatments, a slab of nematic LC can be obtained with a uniform alignment of the LC director. Such a sample exhibits uniaxial optical symmetry with two principal refractive indices n_o and n_e. The ordinary refractive index n_o is for light with electric field polarization perpendicular to the director and the extraordinary refractive index n_e is for light with electric field polarization parallel to the LC director [15]. If the incident light is polarized at an angle theta with respect to the LC director, we can define the effective refractive index n_{eff} as follows :

$$n_{eff}(\theta) = \frac{n_e n_o}{\sqrt{n_o^2 \cos^2\theta + n_e^2 \sin^2\theta}} \tag{1.1}$$

Here, the birefringence (or optical anisotropy) is defined as

$$\Delta n = n_e - n_o \tag{1.2}$$

If $n_o < n_e$, the LC is said to be positive birefringent, whereas if $n_e < n_o$, it is said to be negative birefringent. Most LCs with rodlike molecules exhibit positive birefringence ranging from 0.05 to 0.45 [15].

1.3. Liquid Crystal Infiltrated Tunable Photonic Crystal Laser

Once PhC structures are constructed, both the PBG structure and lasing mode are decided and are not changeable. However, if we infiltrate LCs into the air holes of the PhC structure, the dielectric constant configuration changes as the LC arrangement changes. Consequently, the PBG structure and lasing mode also change [8].

In recent years, the LC infiltrated tunable 2D PhC laser has been studied both theoretically and experimentally [10,11]. In these researches, the laser wavelength shift, lasing mode and quality factor change were reported.

Until now, two kinds of methods in changing LC arrangement, which are electrical and optical, have been reported [10,11]. Two different types of tuning are illustrated in the Figure 1.5. In the electrical tuning method, electric fields are applied perpendicularly through the 2D PhC slab, and the arrangement of LCs changes. In the optical tuning method, the reorientation of LCs occurs by triggering photo addressable polymer (PAP) film using PAP writing laser [11].

Compared to the experimental progress, the computational simulations of LC infiltrated tunable PhC laser are disappointing since they are commonly assuming LCs as optically isotropic materials with their effective refractive indices. Due to this rough assumption, the exact analysis was not possible and there were possibilities of missing important properties.

Therefore, we've developed the FDTD program which can simulate the light propagation in LC medium. Using this, we will analyze the characteristics of LC infiltrated tunable PhC laser.

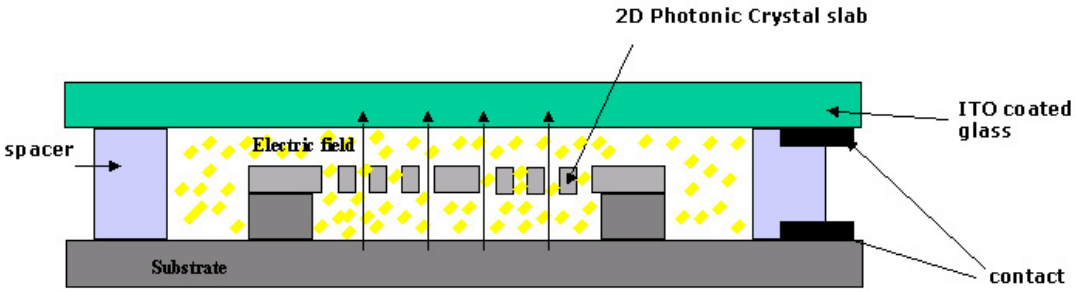

(a) electrical tuning

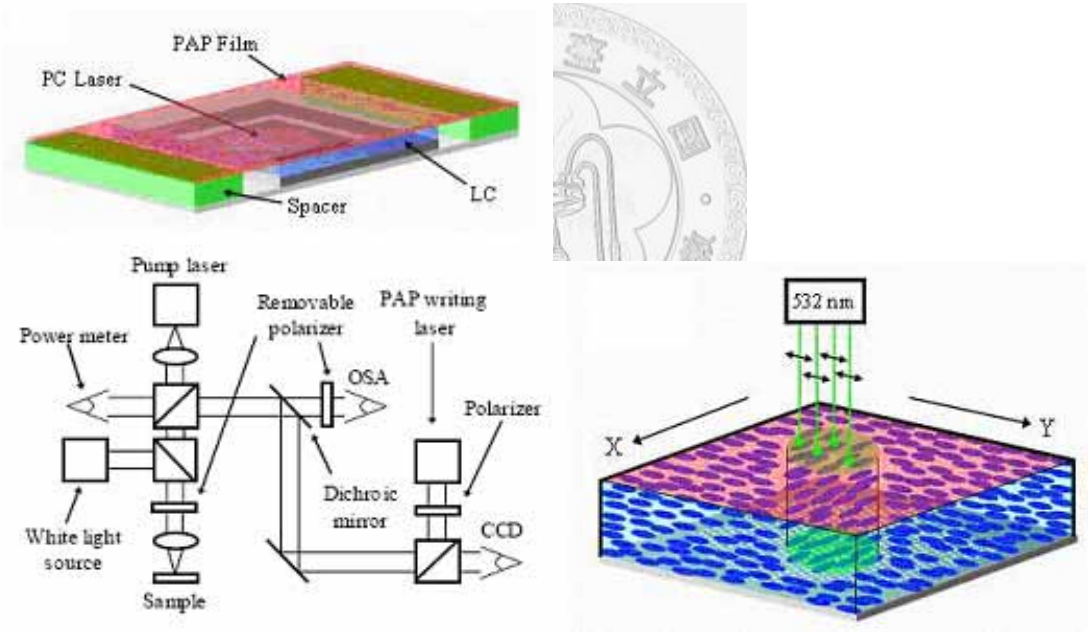

(b) optical tuning (Figure from reference [11])

Figure 1.5 Two kinds of the tuning method

References

[1] E. Yablonovitch, “Inhibited spontaneous emission in solid-stat physics and electronics”, Phys. Rev. Lett. 58, 2059-2062 (1987).

[2] Alongkarn Chutinan and Susumu Noda, “Waveguides and waveguide bends in two dimensional photonic crystal slabs”, Phys. Rev. B 62, 4488-4492 (2000).

[3] S. Noda, A. Chutinan, and M. Imada, “Trapping and emission of photons by a single defect in a photonic bandgap structure”, Nature 407, 608-610 (2000).

[4] O. Painter, R.K. Lee, A. Scherer, A. Yariv, J. D. O’Brien, P. D. Dapkus, and I. Kim, “Two-dimensional photonic band-gap defect mode laser”, Science, 284, 1819-1821 (1999).

[5] Hong-Gyu Park, Se-Heon Kim, Min-Kyo Seo, Young-Gu Ju, Sung-Bock Kim, and Yong-Hee Lee, “Characteristics of Electrically Driven Two-Dimensional Photonic Crystal Lasers”, IEEE J. Quantum Electron., 41 1131 (2005).

[6] T.Yoshi, A.Scherer, J.Hendrickson, G.Khitrova, H. M. Gibbs, G. Rupper, C. Ell, O.B. Schekin, and D. G. Deppe, “Vacuum Rabi splitting with a single quantum dot in a photonic crystal nanocavity”, Nature 432, 200-203 (2004).

[7] A. Badolato, K. Hennessy, M. Atature, J. Dreiser, E. Hu, P. Petroff, and A. Imamoglu, “Deterministic coupling of single quantum dots to single nanocavity modes”, Science 308, 1158-1161 (2005).

[8] Kurt Busch and Sajeev John, “Liquid-Crystal Photonic-Band-Gap Materials: The Tunable Electromagnetic Vacuum”, Phys. Rev. Lett. 83, 967 (1999).

[9] Ryotaro Ozaki, Yuko Matsuhisa, Masanori Ozaki, and Katsumi Yoshino, “Electrically tunable lasing based on defect mode in one-dimensional photonic crystal

with conducting polymer and liquid crystal defect layer", Appl. Phys. Lett. 84, 1844-1846 (2004).

[10] B. Maune, M. Loncar, J. Witzens, M. Hochberg, T. Baehr-Jones, D. Psaltis, A. Scherer, and Y. Qiu, "Liquid crystal electric tuning of a photonic crystal laser," Appl. Phys. Lett. 85, 360-362 (2004).

[11] Brett Maune, Jeremy Witzens, Thomas Baehr-Jones, Michael Kolodrubetz, Harry Atwater, and Axel Scherer, Rainer Hagen, Yueming Qiu, "Optically triggered Q-switched photonic crystal Laser", OPTICS EXPRESS 13, 4699 (2005).

[12] John D. Joannopoulos, Robert D. Meade, and Joshua N. Winn, *Photonic Crystals: Molding the Flow of Light*, Princeton University Press (1995).

[13] Hong-Gyu Park, Jeong-Ki Hwang, Joon Huh, Han-Youl Ryu, Se-Heon Kim, Jeong-Soo Kim, and Yong-Hee Lee, "Characteristics of Modified Single-Defect Two-Dimensional Photonic Crystal Lasers", IEEE JOURNAL OF QUANTUM ELECTRONICS 38, 1353 (2002).

[14] Y. Akahane, T. Asano, B. S. Song and S. Noda, "High-Q photonic nanocavity in a two-dimensional photonic crystal", *Nature* **425,** 944–947 (2003).

[15] Pochi Yeh and Claire Gu, *Optics of Liquid Cyrstal Displays*, Wiley Interscience (1999).

[16] Peter J. Collings and Michael Hird, *Introduction to Liquid Crystals*, Taylor & Francis (1997).

Chapter 2.

Simulation of Light Propagation using Finite-Difference Time-Domain method

To simulate the light propagation in the LC infiltrated 2D PhC laser structure, we will use the Finite-Difference Time-Domain (FDTD) method. “Finite-Difference Time-Domain method” is the method which can simulate electromagnetic phenomena using finite-difference expressions of Maxwell Equation. This method is widely used to simulate the electromagnetic phenomena from atomic levels to microwave levels [1].

In this chapter, we will briefly introduce the principle of FDTD method used in our simulation. And using this FDTD method, we will analyze the light propagation in both non-birefringent materials and birefringent materials to test the reliability of the method before simulating LC infiltrated 2D PhC laser.

2.1. Finite-Difference Time-Domain (FDTD) Method

To simulate the light propagation in discrete computation domain, we need to know the first principle of the light propagation, which is called “Maxwell equations”, and convert them into the finite-difference expressions.

In the non-absorptive, non-magnetic and currentless medium ($J = 0$, $\sigma = 0$, $\mu = \mu_0$), Maxwell equations are expressed as following equations:

$$\nabla \times \vec{H} = \varepsilon \frac{\partial \vec{E}}{\partial t} \qquad \text{(Ampere's Law)}$$

$$\nabla \times \vec{E} = -\mu_0 \frac{\partial \vec{H}}{\partial t} \qquad \text{(Faraday's Law)}$$

$$\nabla \bullet \vec{D} = \rho$$

$$\nabla \bullet \vec{B} = 0 \qquad (2.1)$$

To convert these equations into finite-difference expressions, we assume a discrete computational domain whose unit cell size is Δx , Δy , Δz , Δt in x, y, z spatial directions and a time direction, respectively. Now we can denote every space-time grid point as (i,j,k;n), which represents (i Δx ,j Δy ,k Δz ; n Δt) (i,j,k are integer).

Here, We adopt well-known Yee Grid [1]. Yee Grid assumes that the E fields and H fields in (i,j,k;n) unit cell represents the values at the points illustrated in Figure 2.1 and they are mismatched by 1/2 time step (i.e. E-fields are defined only at (n+1/2) Δt , while H-fields are defined only at n Δt).

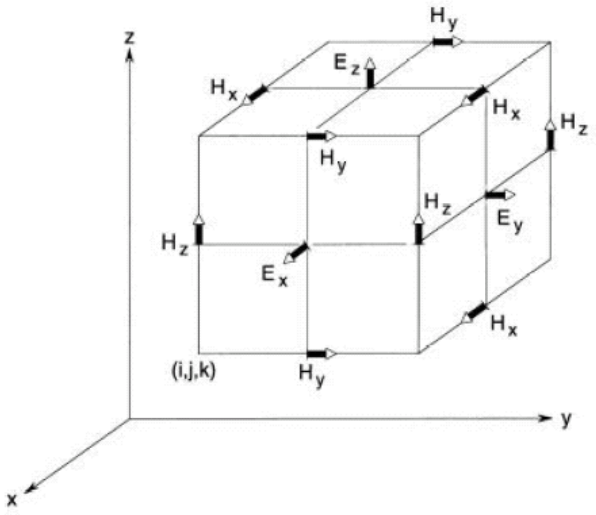

Figure 2.1 Yee Grid

Furthermore, the spatial size of each side in unit cells should be less than 1/10 of wavelength for the rigorous calculation and one time step should be less than $\frac{1}{c\sqrt{(1/\Delta x)^2+(1/\Delta y)^2+(1/\Delta z)^2}}$ for numerical stability [1]. In this research, we set $\Delta t=\frac{\Delta x}{2c}\le\frac{\Delta x}{c\sqrt{3}}$ assuming $\Delta x=\Delta y=\Delta z$.

In addition to Yee Grid, we will use the following two approximation equations.[1]

1. Central difference expressions

$$\frac{\partial u|_{i,j,k}^{n}}{\partial x}=\frac{u|_{i+1/2,j,k}^{n}-u|_{i-1/2,j,k}^{n}}{\Delta x}+O[(\Delta x)^2]$$

$$\frac{\partial u|_{i,j,k}^{n}}{\partial t}=\frac{u|_{i,j,k}^{n+1/2}-u|_{i,j,k}^{n-1/2}}{\Delta t}+O[(\Delta t)^2] \qquad (2.2)$$

2. Semi-implicit approximation

$$u|_{i,j,k}^{n}=\frac{u|_{i,j,k}^{n+1/2}+u|_{i,j,k}^{n-1/2}}{2} \qquad (2.3)$$

where $u|_{i,j,k}^{n}\equiv u(i\Delta x, j\Delta y, k\Delta z, n\Delta t)$, any functions of space and time evaluated at a discrete point in the grid and at a discrete point in time.

Now, we can change Maxwell equations (Ampere's law and Faraday's law) into the finite-difference expressions as following.

(Ampere's Law)

$$\frac{E_x\big|_{i,j+1/2,k+1/2}^{n+1/2} - E_x\big|_{i,j+1/2,k+1/2}^{n-1/2}}{\Delta t} = \varepsilon_{i,j+1/2,k+1/2}^{-1}\left[\frac{H_z\big|_{i,j+1,k+1/2}^{n} - H_z\big|_{i,j,k+1/2}^{n}}{\Delta y} - \frac{H_y\big|_{i,j+1/2,k+1}^{n} - H_y\big|_{i,j+1/2,k}^{n}}{\Delta z}\right]$$

$$\frac{E_y\big|_{i-1/2,j+1,k+1/2}^{n+1/2} - E_y\big|_{i-1/2,j+1,k+1/2}^{n-1/2}}{\Delta t} = \varepsilon_{i-1/2,j+1,k+1/2}^{-1}\left[\frac{H_x\big|_{i-1/2,j+1,k+1}^{n} - H_x\big|_{i-1/2,j+1,k}^{n}}{\Delta z} - \frac{H_z\big|_{i,j+1,k+1/2}^{n} - H_z\big|_{i-1,j+1,k+1/2}^{n}}{\Delta x}\right]$$

$$\frac{E_z\big|_{i-1/2,j+1/2,k+1}^{n+1/2} - E_z\big|_{i-1/2,j+1/2,k+1}^{n-1/2}}{\Delta t} = \varepsilon_{i-1/2,j+1/2,k+1}^{-1}\left[\frac{H_y\big|_{i,j+1/2,k+1}^{n} - H_y\big|_{i-1,j+1/2,k+1}^{n}}{\Delta x} - \frac{H_x\big|_{i-1/2,j+1,k+1}^{n} - H_x\big|_{i-1/2,j,k+1}^{n}}{\Delta y}\right]$$

(2.4)

(Faraday's Law)

$$\frac{H_x\big|_{i-1/2,j+1,k+1}^{n+1} - H_x\big|_{i-1/2,j+1,k+1}^{n}}{\Delta t} = \mu_0^{-1}\left[\frac{E_y\big|_{i-1/2,j+1,k+3/2}^{n+1/2} - E_y\big|_{i-1/2,j+1,k+1/2}^{n+1/2}}{\Delta z} - \frac{E_z\big|_{i-1/2,j+3/2,k+1}^{n+1/2} - E_z\big|_{i-1/2,j+1/2,k+1}^{n+1/2}}{\Delta y}\right]$$

$$\frac{H_y\big|_{i,j+1/2,k+1}^{n+1} - H_y\big|_{i,j+1/2,k+1}^{n}}{\Delta t} = \mu_0^{-1}\left[\frac{E_z\big|_{i+1/2,j+1/2,k+1}^{n+1/2} - E_z\big|_{i-1/2,j+1/2,k+1}^{n+1/2}}{\Delta x} - \frac{E_x\big|_{i,j+1/2,k+3/2}^{n+1/2} - E_x\big|_{i,j+1/2,k+1/2}^{n+1/2}}{\Delta z}\right]$$

$$\frac{H_z\big|_{i,j+1,k+1/2}^{n+1} - H_z\big|_{i,j+1,k+1/2}^{n}}{\Delta t} = \mu_0^{-1}\left[\frac{E_x\big|_{i,j+3/2,k+1/2}^{n+1/2} - E_x\big|_{i,j+1/2,k+1/2}^{n+1/2}}{\Delta y} - \frac{E_y\big|_{i+1/2,j+1,k+1/2}^{n+1/2} - E_y\big|_{i-1/2,j+1,k+1/2}^{n+1/2}}{\Delta x}\right]$$

(2.5)

From eq. (2.4) and eq. (2.5), we can get the update equations for the electromagnetic wave propagation.

(Update Equations)

$$\begin{bmatrix} E_x\big|_{i,j+1/2,k+1/2}^{n+1/2} \\ E_y\big|_{i-1/2,j+1,k+1/2}^{n+1/2} \\ E_z\big|_{i-1/2,j+1/2,k+1}^{n+1/2} \end{bmatrix} = \frac{\varepsilon^{-1}\Delta t}{\Delta x}\begin{bmatrix} H_z\big|_{i,j+1,k+1/2}^{n} - H_z\big|_{i,j,k+1/2}^{n} - \left\{H_y\big|_{i,j+1/2,k+1}^{n} - H_y\big|_{i,j+1/2,k}^{n}\right\} \\ H_x\big|_{i-1/2,j+1,k+1}^{n} - H_x\big|_{i-1/2,j+1,k}^{n} - \left\{H_z\big|_{i,j+1,k+1/2}^{n} - H_z\big|_{i-1,j+1,k+1/2}^{n}\right\} \\ H_y\big|_{i,j+1/2,k+1}^{n} - H_y\big|_{i-1,j+1/2,k+1}^{n} - \left\{H_x\big|_{i-1/2,j+1,k+1}^{n} - H_x\big|_{i-1/2,j,k+1}^{n}\right\} \end{bmatrix} \quad (2.6)$$

$$\begin{bmatrix} H_x\big|_{i-1/2,\,j+1,\,k+1}^{n+1} \\ H_y\big|_{i,\,j+1/2,\,k+1}^{n+1} \\ H_z\big|_{i,\,j+1,\,k+1/2}^{n+1} \end{bmatrix} = \frac{\mu_0^{-1}\Delta t}{\Delta x} \begin{bmatrix} E_y\big|_{i-1/2,\,j+1,\,k+3/2}^{n+1/2} - E_y\big|_{i-1/2,\,j+1,\,k+1/2}^{n+1/2} - \left\{ E_z\big|_{i-1/2,\,j+3/2,\,k+1}^{n+1/2} - E_z\big|_{i-1/2,\,j+1/2,\,k+1}^{n+1/2} \right\} \\ E_z\big|_{i+1/2,\,j+1/2,\,k+1}^{n+1/2} - E_z\big|_{i-1/2,\,j+1/2,\,k+1}^{n+1/2} - \left\{ E_x\big|_{i,\,j+1/2,\,k+3/2}^{n+1/2} - E_x\big|_{i,\,j+1/2,\,k+1/2}^{n+1/2} \right\} \\ E_x\big|_{i,\,j+3/2,\,k+1/2}^{n+1/2} - E_x\big|_{i,\,j+1/2,\,k+1/2}^{n+1/2} - \left\{ E_y\big|_{i+1/2,\,j+1,\,k+1/2}^{n+1/2} - E_y\big|_{i-1/2,\,j+1,\,k+1/2}^{n+1/2} \right\} \end{bmatrix} \tag{2.7}$$

Especially, in the birefringent materials such as LCs, dielectric tensor has off-diagonal terms. The dielectric tensor of nematic (uniaxial) LCs given in the laboratory (x,y,z) coordinate system is as follows [2].

$$\varepsilon = \begin{pmatrix} \varepsilon_{xx} & \varepsilon_{xy} & \varepsilon_{xz} \\ \varepsilon_{yx} & \varepsilon_{yy} & \varepsilon_{yz} \\ \varepsilon_{zx} & \varepsilon_{zy} & \varepsilon_{zz} \end{pmatrix} \tag{2.8}$$

$$\begin{aligned} \varepsilon_{xx} &= n_o^2 + \left(n_e^2 - n_o^2\right)\sin^2\theta_c \cos^2\phi_c \\ \varepsilon_{xy} &= \varepsilon_{yx} = \left(n_e^2 - n_o^2\right)\sin^2\theta_c \sin\phi_c \cos\phi_c \\ \varepsilon_{xz} &= \varepsilon_{zx} = \left(n_e^2 - n_o^2\right)\sin\theta_c \cos\theta_c \cos\phi_c \\ \varepsilon_{yy} &= n_o^2 + \left(n_e^2 - n_o^2\right)\sin^2\theta_c \sin^2\phi_c \\ \varepsilon_{yz} &= \varepsilon_{zy} = \left(n_e^2 - n_o^2\right)\sin\theta_c \cos\theta_c \sin\phi_c \\ \varepsilon_{zz} &= n_o^2 + \left(n_e^2 - n_o^2\right)\cos^2\theta_c \end{aligned}$$

where n_o and n_e are the ordinary and extraordinary indices of refraction of the LC medium, θ_c is the angle between the LC director and the z axis, and ϕ_c is the angle between the projection of the LC director on the xy plane and the x axis (Figure 1.4)

Therefore, the update equations for the LC medium become eq. (2.9) and eq. (2.10) in the next page.

$$\begin{bmatrix} E_x\big|_{i,j+1/2,k+1/2}^{n+1/2} \\ E_y\big|_{i-1/2,j+1,k+1/2}^{n+1/2} \\ E_z\big|_{i-1/2,j+1/2,k+1}^{n+1/2} \end{bmatrix} = \frac{\Delta t}{\Delta x}\frac{1}{(\varepsilon_{xx}\varepsilon_{yz}\varepsilon_{zy}+\varepsilon_{yx}\varepsilon_{xy}\varepsilon_{zz}+\varepsilon_{zx}\varepsilon_{xz}\varepsilon_{yy}-\varepsilon_{xx}\varepsilon_{yy}\varepsilon_{zz}-\varepsilon_{yx}\varepsilon_{xz}\varepsilon_{zy}-\varepsilon_{zx}\varepsilon_{xy}\varepsilon_{yz})}\times$$

$$\begin{pmatrix} \varepsilon_{yz}\varepsilon_{zy}-\varepsilon_{yy}\varepsilon_{zz} & \varepsilon_{xy}\varepsilon_{zz}-\varepsilon_{xz}\varepsilon_{zy} & \varepsilon_{xz}\varepsilon_{yy}-\varepsilon_{xy}\varepsilon_{yz} \\ \varepsilon_{yx}\varepsilon_{zz}-\varepsilon_{yz}\varepsilon_{zx} & \varepsilon_{xz}\varepsilon_{zx}-\varepsilon_{xx}\varepsilon_{zz} & \varepsilon_{xx}\varepsilon_{yz}-\varepsilon_{xz}\varepsilon_{yx} \\ \varepsilon_{yy}\varepsilon_{zx}-\varepsilon_{yx}\varepsilon_{zy} & \varepsilon_{xx}\varepsilon_{zy}-\varepsilon_{xy}\varepsilon_{zx} & \varepsilon_{xy}\varepsilon_{yx}-\varepsilon_{xx}\varepsilon_{yy} \end{pmatrix}\begin{bmatrix} H_z\big|_{i,j+1,k+1/2}^{n}-H_z\big|_{i,j,k+1/2}^{n}-\left\{H_y\big|_{i,j+1/2,k+1}^{n}-H_y\big|_{i,j+1/2,k}^{n}\right\} \\ H_x\big|_{i-1/2,j+1,k+1}^{n}-H_x\big|_{i-1/2,j+1,k}^{n}-\left\{H_z\big|_{i,j+1,k+1/2}^{n}-H_z\big|_{i-1,j+1,k+1/2}^{n}\right\} \\ H_y\big|_{i,j+1/2,k+1}^{n}-H_y\big|_{i-1,j+1/2,k+1}^{n}-\left\{H_x\big|_{i-1/2,j+1,k+1}^{n}-H_x\big|_{i-1/2,j,k+1}^{n}\right\} \end{bmatrix}$$

(2.9)

$$\begin{bmatrix} H_x\big|_{i-1/2,j+1,k+1}^{n+1} \\ H_y\big|_{i,j+1/2,k+1}^{n+1} \\ H_z\big|_{i,j+1,k+1/2}^{n+1} \end{bmatrix} = \frac{\mu_0^{-1}\Delta t}{\Delta x}\begin{bmatrix} E_y\big|_{i-1/2,j+1,k+3/2}^{n+1/2}-E_y\big|_{i-1/2,j+1,k+1/2}^{n+1/2}-\left\{E_z\big|_{i-1/2,j+3/2,k+1}^{n+1/2}-E_z\big|_{i-1/2,j+1/2,k+1}^{n+1/2}\right\} \\ E_z\big|_{i+1/2,j+1/2,k+1}^{n+1/2}-E_z\big|_{i-1/2,j+1/2,k+1}^{n+1/2}-\left\{E_x\big|_{i,j+1/2,k+3/2}^{n+1/2}-E_x\big|_{i,j+1/2,k+1/2}^{n+1/2}\right\} \\ E_x\big|_{i,j+3/2,k+1/2}^{n+1/2}-E_x\big|_{i,j+1/2,k+1/2}^{n+1/2}-\left\{E_y\big|_{i+1/2,j+1,k+1/2}^{n+1/2}-E_y\big|_{i-1/2,j+1,k+1/2}^{n+1/2}\right\} \end{bmatrix} \quad (2.10)$$

Here, if we know the H-fields at $t = n\Delta t$, we can obtain E-fields at $t = (n+1/2)\Delta t$ by eq. (2.9). Similarly, if we know the E fields at $t = (n+1/2)\Delta t$, we can obtain the H-fields at $t = (n+1)\Delta t$ by eq. (2.10). In this way, we can get E-fields and H-fields at every space-time grid point as t increases. Figure 2.2 illustrates this algorithm.

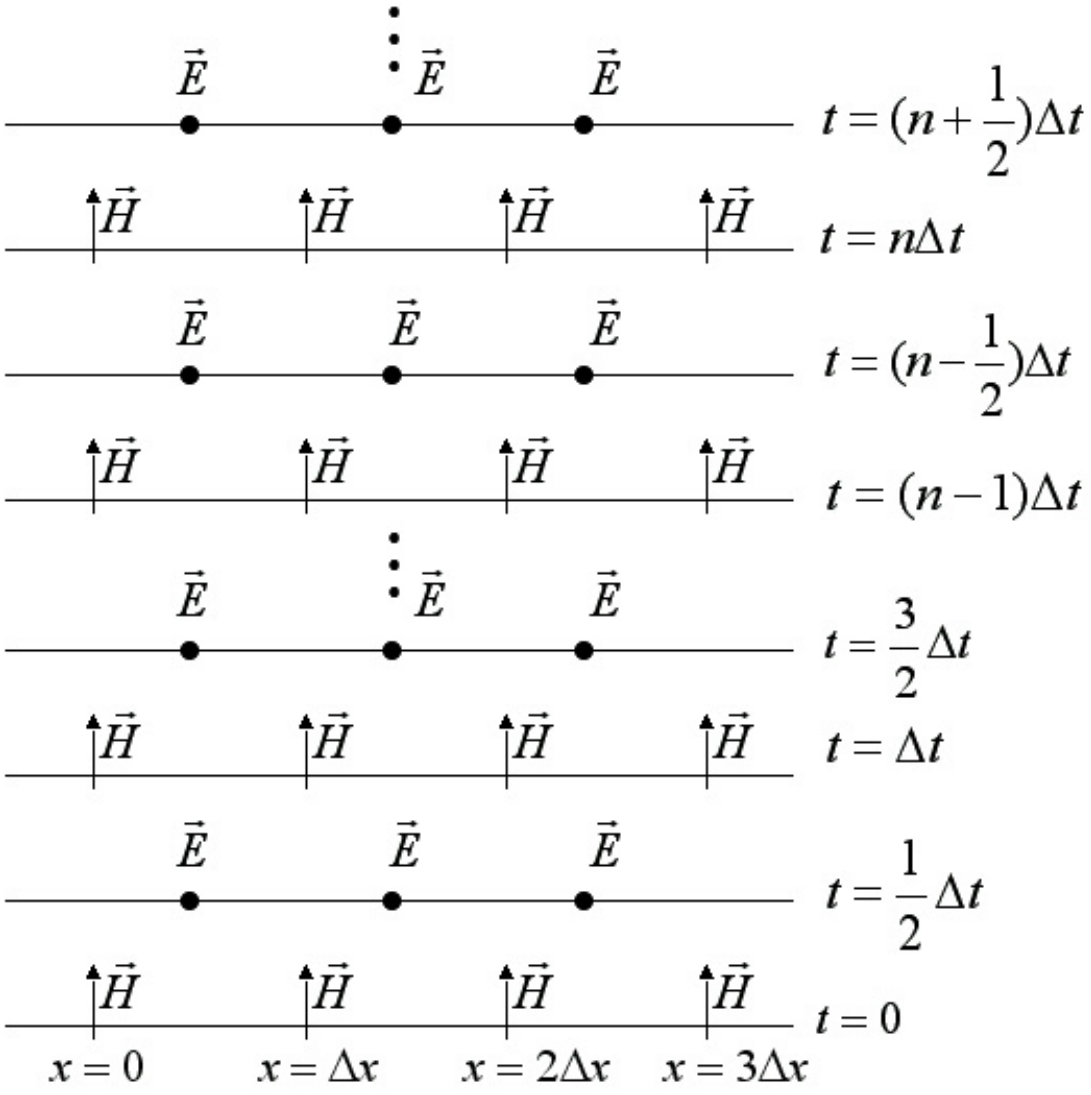

Figure 2.2 Space-time chart of Yee Algorithm for 1D wave propagation

2.2. Simulation of Light Propagation

In the previous section, we have seen the basics of Finite-Difference Time-Domain (FDTD) method. In order to confirm the reliability of this simulation method, we will analyze the simulation results of light propagation in air and LC medium.

Here, the spatial grid size is $\Delta x = 22.5nm$ which is about the molecular length of liquid crystals and the corresponding time step size, determined by the numerical stability condition of FDTD method, is $\Delta t = 3.75 \times 10^{-17} s$.

2.2.1 Light propagation in air

First, let' s see the simulation results of the light propagation in air. The refractive index of the air is 1 (n=1) and it is optically isotropic. As we can see in Figure 2.3, the sine wave has the wavelength of 1550nm ($= n_{air} \times 1550nm$) and propagates 4.5 μm ($\approx \frac{c}{n_{eff}} \Delta t = \frac{3 \times 10^8 m/s}{1.0} \times 15 fs$) in 15 fs, which agrees with the real light propagation properties.

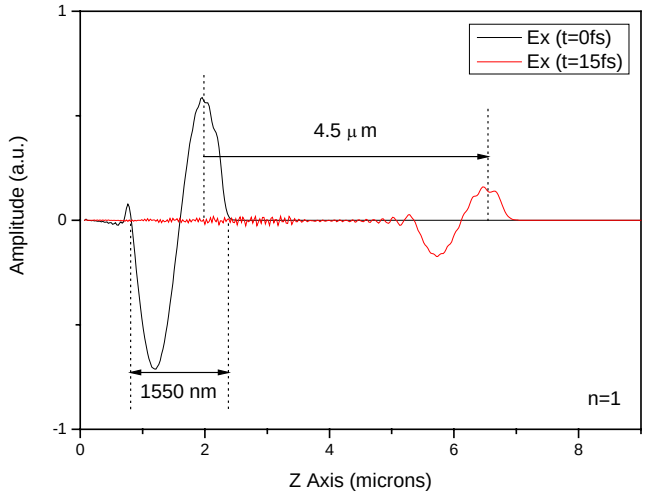

Figure 2.3 Light propagation in air

2.2.2 Light propagation in Nematic Liquid Crystal

Now, let's see the light propagation in nematic LC. In our simulation, we assume the LC has $n_o = 1.5$, $n_e = 1.8$, and the propagating wave has the wavelength of 1550nm.

Figure 2.4-(a) shows the propagation of the light, which is polarized parallel to the LC director, i.e. $n_{eff} = n_e$. We can notice that the wave has the wavelength of 1550nm ($\approx n_e \times 860nm$) and propagates 2.5 μm ($\approx \frac{c}{n_{eff}} \Delta t = \frac{3\times10^8 m/s}{1.8} \times 15\, fs$) in 15 fs.

In the case of Figure 2.4-(b), the light is polarized perpendicular to the LC director and the effective refractive index becomes $n_{eff} = n_o$. Again, we can notice that the wave has the wavelength of 1550nm ($\approx n_o \times 1035nm$) and propagates 3.0 μm ($\approx \frac{c}{n_{eff}} \Delta t = \frac{3\times10^8 m/s}{1.5} \times 15\, fs$) in 15 fs. These simulation results well agrees with the

known light propagating properties in LC medium.

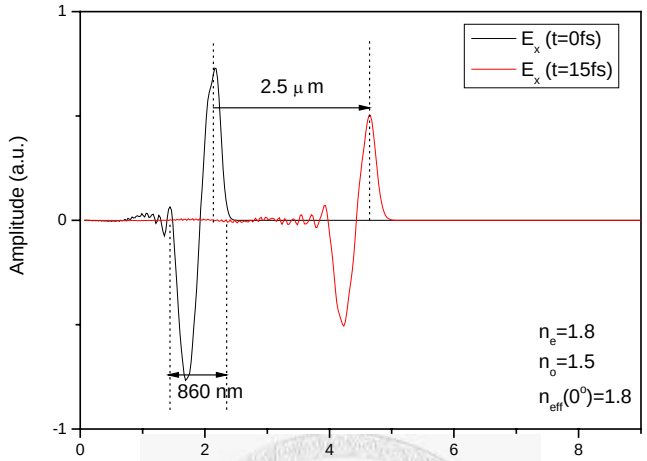

(a) $n_{eff} = n_e$

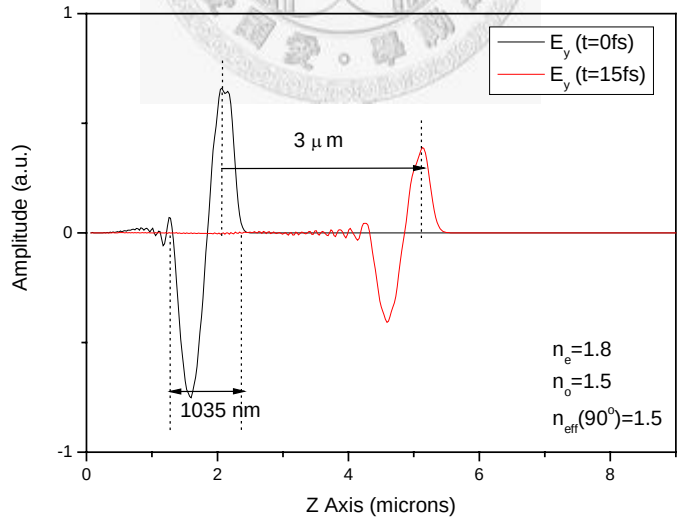

(b) $n_{eff} = n_o$

Figure 2.4 Light propagation in nematic LC

2.2.3. Light propagation in Twisted Nematic Liquid Crystal

For the last step of testing our FDTD simulator, we simulate the light propagation through the 90° twisted nematic LC cell (90° TN cell). Here, we assume E_x polarized wave propagates from left to right, and the nematic LCs with n_e=1.6, n_o=1.5 are uniformly twisted in the 2 μm-90° TN LC cell as illustrated in Figure 2.5.

Before the wave reached at the 90° TN LC cell (t=0 *fs*), there is only E_x fields on the left of the 90° TN LC cell (Figure 2.5). As the wave propagates through the 90° TN LC cell (t=5.625 *fs*, 11.25 *fs*), E_y fields are generated. After the wave passes E_y Analyzer (t=26.25 *fs*), only E_y fields exist on the right of the 90° TN LC cell, and there is reflected wave propagating to the left in the 90° TN LC cell.

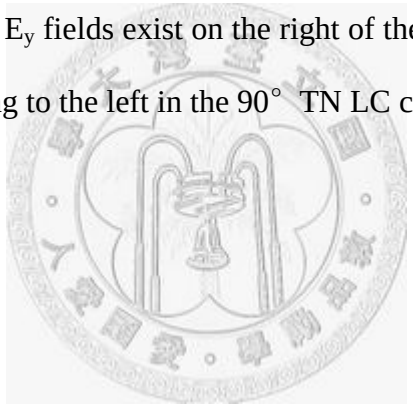

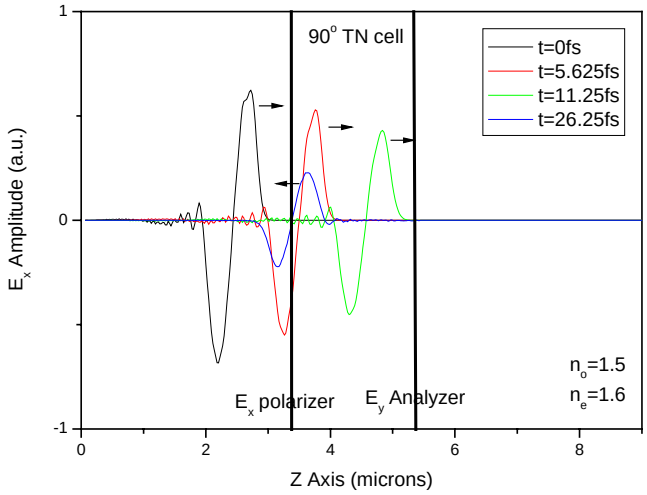

(a) E_x profile

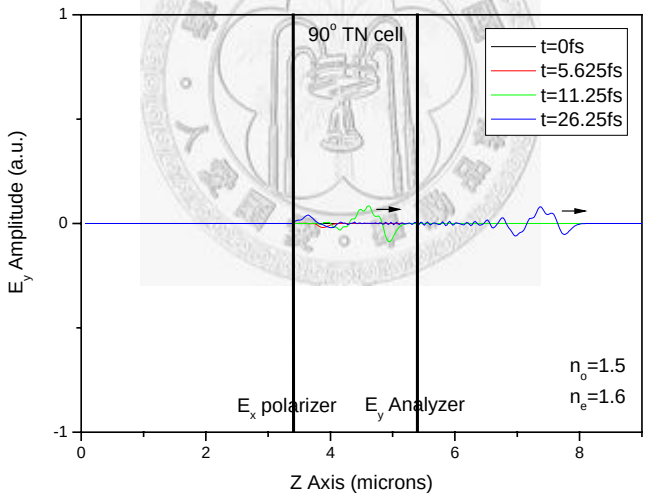

(b) E_y profile

Figure 2.5　Light propagation through the 90° TN LC cell

References

[1] A. Taflove and Susan C. Hagness, *Computational Electrodynamics—The Finite-Difference Time-Domain Method*, 2nd ed., Artech House (2000).

[2] Pochi Yeh and Claire Gu, *Optics of Liquid Cyrstal Displays*, Wiley Interscience (1999).

Chapter 3.

Design of the Liquid Crystal Infiltrated Photonic Crystal Laser

Before LC infiltrated PhC laser can be constructed, several parameters must be carefully designed. In this chapter, we'll discuss the choice of the proper LC and several PhC slab parameters, such as a lattice constant (a), air hole radius (r), slab thickness (t) and defect shape.

3.1. Choice of the Liquid Crystal

LCs with larger birefringence gives larger refractive index tuning ranges. However, infiltrating LCs into the air holes of 2D PhC slab decreases the refractive index contrast of the system, and this lowering of refractive index contrast narrows the PBG. Thus, both in-plane and vertical confinement of the light decrease, which means the reduction of the cavity's quality (Q) factor. Moreover, their large birefringence can scatter light if LCs are not aligned uniformly [1]. Therefore, we have to choose a LC that is well-ordered nematic LC for good uniformity and has relatively low refractive index with modest birefringence.

After this considerations about LCs, the LC chosen for this simulation is Merck E-7 which is nematic at room temperature and has n_e=1.75, n_o=1.5231. at λ=577nm (Table 3.1).

Table 3.1 Merck E7

λ (nm)	n_e	n_o
577	1.75	1.5231
589.3	1.7462	1.5216
632.8	1.7371	1.5183

Since we are interested in the 2D PhC laser near the communicational wavelength of 1550nm, we need n_e and n_o values at 1550nm. By using Cauchy's formula, we can easily obtain these values approximately [2,3].

(Cauchy's Formula) $$n_o = A_o + \frac{B_o}{\lambda^2}\ ,\ n_e = A_e + \frac{B_e}{\lambda^2} \tag{3.1}$$

Inserting the values at three different wavelengths (table 3.1) into the above formula, we can calculate the coefficients A_e, B_e, A_o, B_o, and the obtained refractive indices at λ=1550nm are $n_e \approx 1.6841$, $n_o \approx 1.4986$.

3.2. Design of the 2D Photonic Crystal Slab

In this section, we will consider several important parameters of the 2D PhC slab structure. Here, we assume the slab material is InGaAsP quantum well material whose effective dielectric constant is 11.56 at its resonant wavelength 1550nm and the triangular lattice is used for the PhC structure.

3.2.1 Slab thickness

The slab thickness t is one of the important parameters determining the property of the lasing modes. In general, as t increases, the Q factor and the volume of the modes increase together. Thus, to satisfy the single-mode condition and the high Q-factor simultaneously, t should be optimized and $t \sim 0.5a$ is the optimum condition [4].

Since we will fill LCs into the air holes of 2D PhC slab, there is another problem about LC anchoring on the slab [1,5]. To minimize this problem, we should make the slab as thin as possible.

Therefore, considering the single-mode condition, the high Q-factor and the LC anchoring problem, the slab thickness of $t \sim 0.45a$ is suitable and will be used throughout this research.

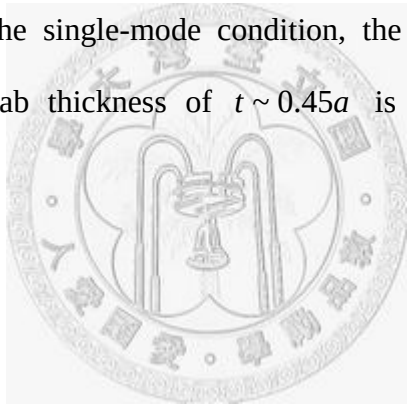

3.2.2 Hole Radius

If the hole radius is too small, LCs in the hole are hard to change their arrangement due to the size of the LC molecules and anchoring energy between LC molecules and InGaAsP slab material [1]. Thus, in order to optimize the hole radius, we will compare only three large radius cases, $r = 0.3a$, $r = 0.35a$, $r = 0.4a$, using 3D Plane Wave Expansion (PWE) method.

In Figure 3.1, the calculated photonic band structures for three different hole radii are given. In the figure (b)~(d), two TE-like photonic band structures, which are representing the cases that the LCs are regarded as non-birefringent materials of $n_{eff} = n_e$ and $n_{eff} = n_o$, are drawn together. PBG and the gap-midgap ratio are defined

in this hybrid band structure. Here, we assume slab thickness $t = 0.45a$ and the TM-like mode is excluded due to its low gap-midgap ratio.

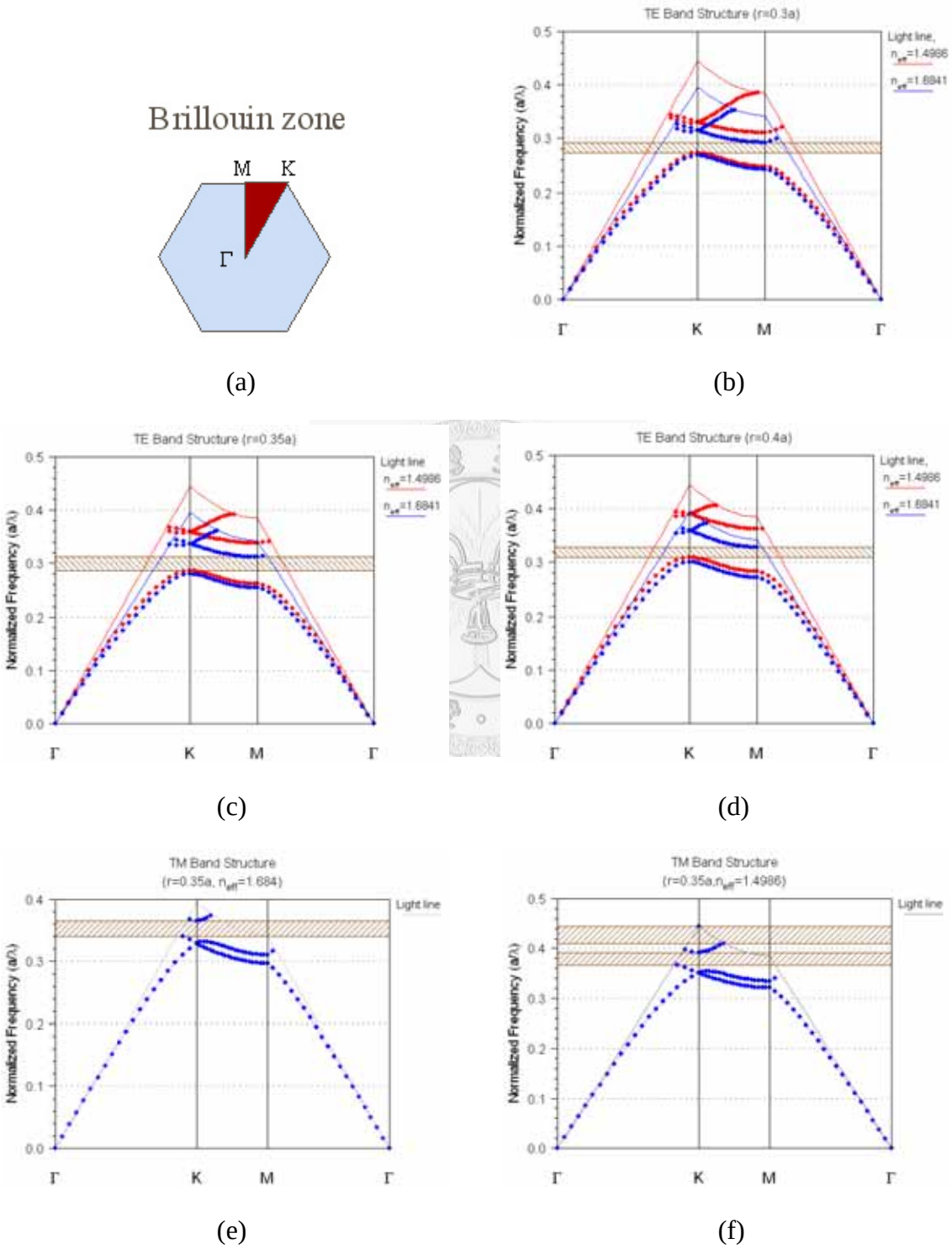

Fig. 3.1 Photonic band structures at different hole radii and n_{eff}

Table 3.2 PBG ranges and gap-midgap ratios at the TE-like mode

	PBG range at $n_{eff} = n_o$ (unit : a/λ)	PBG range $n_{eff} = n_e$ (unit : a/λ)	Gap-midgap ratio $(\frac{\Delta f}{f_{midgap}})$
$r = 0.3a$	**0.27263**~0.31072	0.26816~**0.29241**	0.07
$r = 0.35a$	**0.28587**~0.33773	0.27992~**0.31168**	0.08639
$r = 0.4a$	**0.30988**~0.36219	0.30048~**0.32797**	0.05672

From the Figure 3.2 and Table 3.2, we could notice $r = 0.35a$ with the largest gap-midgap ratio is the optimum condition among the three different radii. Here, since the dielectric constant contrast is decreased by infiltrated LCs, gap-midgap ratios are small compared to ordinary air-hole PhC structures. However, the real gap-midgap ratios are larger than the calculated value since we assumed two extreme cases of $n_{eff} = n_o$ and $n_{eff} = n_e$. In the figure (e) and (f), TM-like photonic band structures are shown for reference.

3.2.3 Lattice Constant

When $r = 0.35a$, the optimum condition as mentioned above, the PBG appears between a/λ =0.28587 and a/λ =0.31168. Since we are interesting in the wavelength of ~1550nm, $a = 460nm$ is considered the optimum lattice constant, which lies at the center of the PBG.

3.2.4 Defect design

From the previous sections, we determined several important parameters such as slab thickness ($t = 0.45a$), hole radius ($r = 0.35a$) and lattice constant ($a = 460nm$).

In this section, we will design the shape of the defect. Only single defect is considered due to its small modal volume and simpleness.

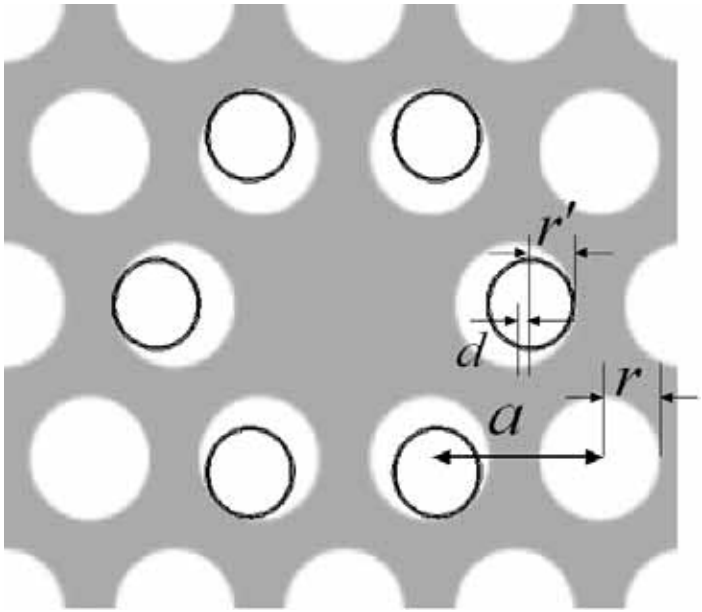

Figure 3.2 Modified parameters d and r'

Modified parameters are shown in Figure 3.2. The radius of the nearest neighbor holes from the single defect is changed to r' and they are pushed away from the defect by d.

Using the PWE method, we found many defect shapes in which resonant modes (Figure 3.3) appear near 1550nm. Among them, three characteristic defect designs (Figure 3.4) are found by the FDTD simulation and only these three defect designs are

discussed in the next chapter.

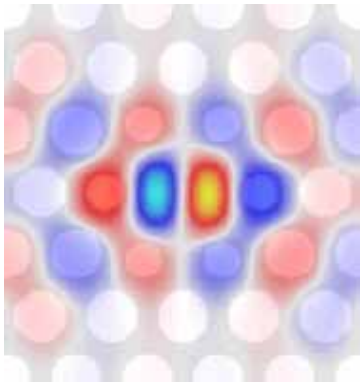

(a) Degenerate dipole modes

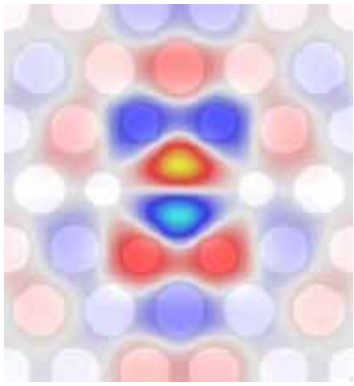

(b) Monopole mode

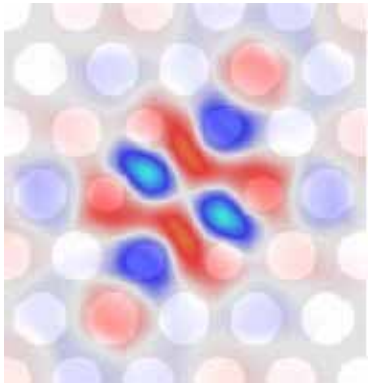

(c) Degenerate quadrupole modes

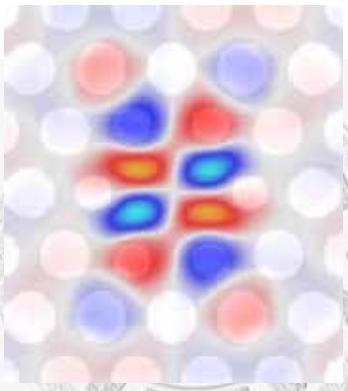

(d) Hexapole mode

Figure 3.3 Various fundamental resonant mode modes (d =0.1a, r' =0.25a)

Design A Design B Design C

Figure 3.4 Charateristic defect designs : Design A ($r' = 0.25a$, $d = 0.13a$),

Design B ($r' = 0.25a$, $d = 0$), Design C ($r' = 0.25a$, $d = 0.17a$)

References

[1] B. Maune, M. Loncar, J. Witzens, M. Hochberg, T. Baehr-Jones, D. Psaltis, A. Scherer, and Y. Qiu, “Liquid crystal electric tuning of a photonic crystal laser,” Appl. Phys. Lett. 85, 360-362 (2004).

[2] S. T. Wu, C. S. Wu, M. Warenghem, and M. Ismaili, Opt. Eng. **32**, 1775 (1993).

[3] S. T. Wu, Phys. Rev. A, 33, 1270 (1986).

[4] Hong-Gyu Park, Jeong-Ki Hwang, Joon Huh, Han-Youl Ryu, Se-Heon Kim, Jeong-Soo Kim, and Yong-Hee Lee, “Characteristics of Modified Single-Defect Two-Dimensional Photonic Crystal Lasers”, IEEE JOURNAL OF QUANTUM ELECTRONICS 38, 1353 (2002).

[5] P. G. de Gennes and J. Prost, *The Physics of Liquid Crystals*, Clarendon Press (1993).

[6] Se-Heon Kim and Yong-Hee Lee, “Symmetry Relations of Two-Dimensional Photonic Crystal Cavity Modes”, IEEE JOURNAL OF QUANTUM ELECTRONICS, 39, 1081 (2003).

Chapter 4.

Characteristics of the Liquid Crystal Infiltrated Tunable Photonic Crystal Laser

In this chapter, we will analyze the simulation results of LC infiltrated tunable 2D PhC laser. Simulation conditions are introduced first and various characteristics in three defect designs, such as single mode laser wavelength shift and laser mode change, are analyzed.

4.1 Simulation Conditions

The simulation domain used in this research is illustrated in Figure 4.1. As mentioned in the previous chapter, InGaAsP quantum well material ($\varepsilon = 11.56$ at $\lambda = 1550\ nm$) is employed as the slab material. Lattice constant (a) is $460\ nm$ and slab thickness is $0.45a$. The hole radius is $0.35a$ except the nearest neighbor holes from the defect. Due to the lack of computing power, we used the simple structure which has 5 hole layers around the center defect. The domain size is $12.5a \times 11a \times 5a$ and the spatial and time steps are assumed to be $\Delta x = 23\ nm$ and $\Delta t = 3.83 \times 10^{-17}\ s$, respectively. At the boundaries of the simulation domain, uniaxial perfectly matched layers (UPML) are placed as an appropriate boundary condition.

LCs are placed at the white part in Figure 4.1. The LC alignment is defined by θ and ϕ in the right inset of Figure 4.1. At the interface of LC medium and the slab

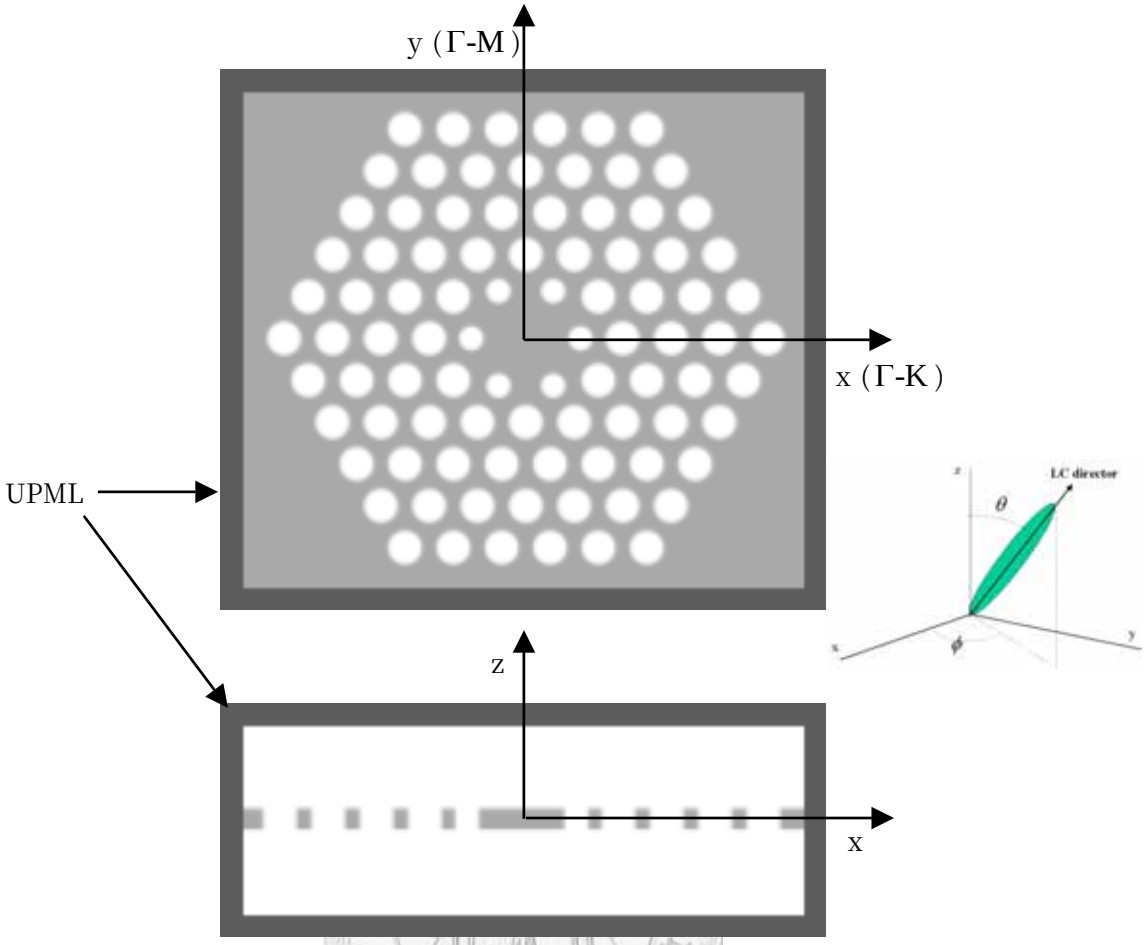

Figure 4.1 The structure of Design A in the simulation domain whose size is $12.5a \times 11a \times 5a$. The alignment of LCs are defined by θ and ϕ.

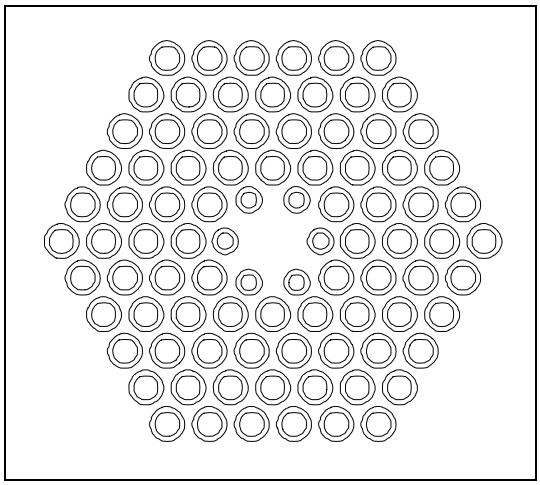

Figure 4.2 Isotropic interface region

material, gradual dielectric change is imposed. This makes the diameter of the tunable LC holes decreased by $\sim 100\,nm$ as shown in Figure 4.2. This isotropic interface region could be regarded as LC anchoring region, yet it is quite rough approximation. In the LC medium excluding the isotropic interface region, LCs are assumed to be uniformly aligned.

The spontaneous dipole emission centered at $1550\,nm$ with FWHM $20\,nm$ is assumed as shown in Figure 4.3 (a), and these dipole sources with random phases are randomly distributed over the slab material in the center circle of diameter $5a$ (Figure 4.3 (b))

All the simulation conditions are same except the defect designs of 2D PhC slab.

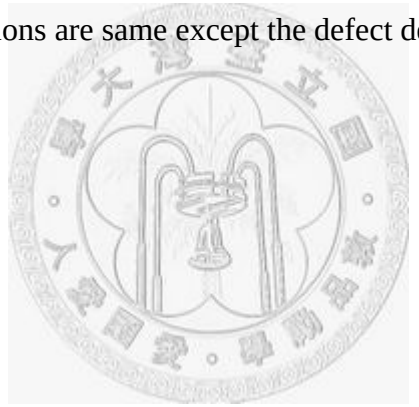

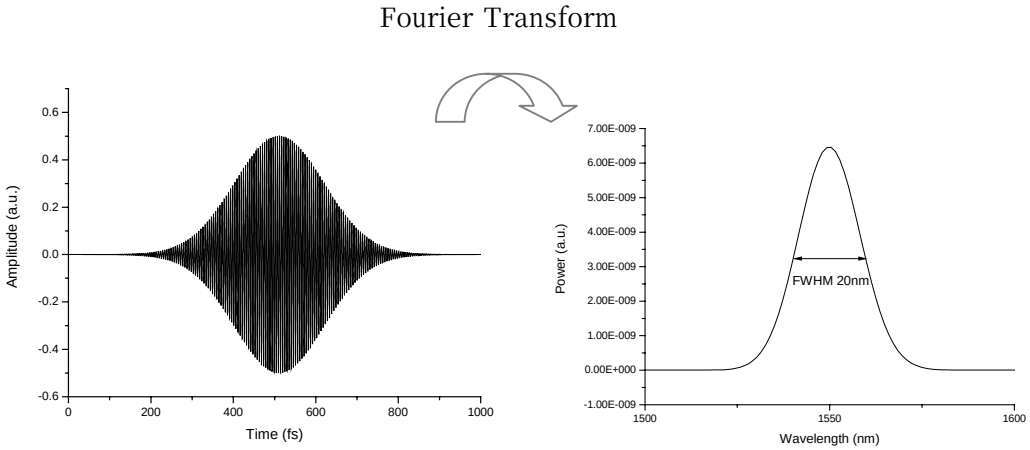

(a)

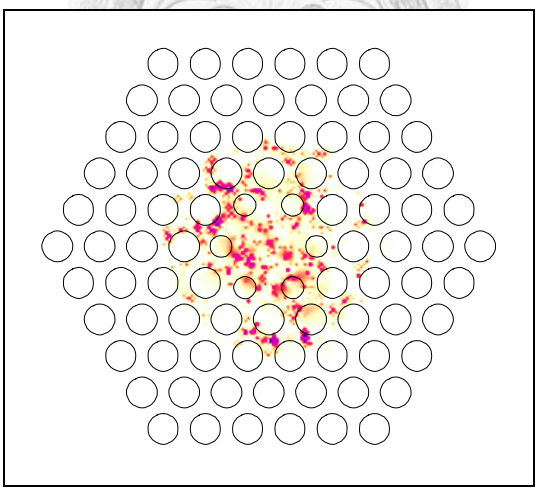

(b)

Figure 4.3 (a) The spontaneous dipole emission centered at $1550\ nm$ with FWHM $20nm$ (b) Random dipole sources in the center circle of $D = 5a$

4.2. Several Characteristics of the Liquid Crystal Infiltrated Photonic Crystal Laser

In this section, we will analyze the simulation results from the three different defect designs (Section 3.2.4) ; Design A ($r' = 0.25a$, $d = 0.13a$), Design B ($r' = 0.25a$, $d = 0$), Design C ($r' = 0.25a$, $d = 0.17a$).

4.2.1. Lasing Wavelength Shift of Single Mode (Design A)

In Design A, as shown in Figure 4.4, the lasing wavelength shifts toward shorter wavelength region (from $1558\,nm$ to $1537\,nm$) as θ changes from 90° to 0°. It seems reasonable compared with the experimental results [1]. We also can notice that the lasing wavelength shift and Q-factor change are not linear to the change of θ. The theoretical Q-factor is 343 when $\theta = 90^\circ, \phi = 0^\circ$, and 539 when $\theta = 0^\circ, \phi = 0^\circ$. It is reasonable that Q-factor increases as θ changes from 90° to 0° since in-plane n_{eff} decreases as the LC director rotates from x-axis to z-axis.

From the H_z field profiles in Figure 4.5, we can find that the lasing mode is the hexapole mode at all the different θ. However, there are differences between the modes. In Figure 4.6, E_x field profile at $\theta = 90^\circ$ is mainly (b), yet there is also another mode which can be known from the oscillation between (c) and (d), while E_x field profile at $\theta = 0^\circ$ does not. This is attributed to the liquid crystal effect by which E_x-polarized light experiences $n_{eff} = n_e$ when LCs are aligned parallel to the x-axis ($\theta = 90^\circ, \phi = 0^\circ$),

$n_{eff} = n_o$ when LCs are aligned parallel to the z-axis ($\theta = 0^\circ$). The same E_y field profiles at (e) and (f) confirm it again.

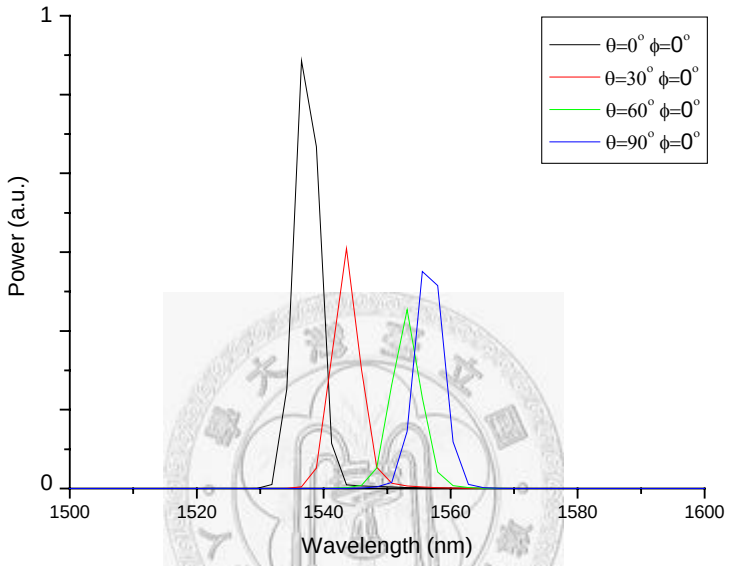

Figure 4.4 Power spectrum (resolution limit : 2.5 *nm*)

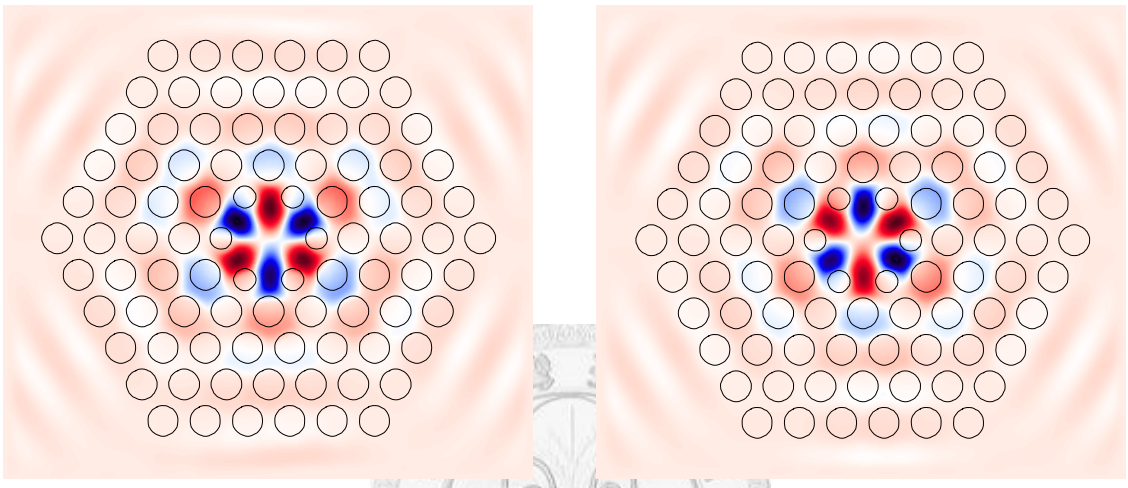

(a) $\theta = 90^\circ$, $\phi = 0^\circ$ (b) $\theta = 60^\circ$, $\phi = 0^\circ$

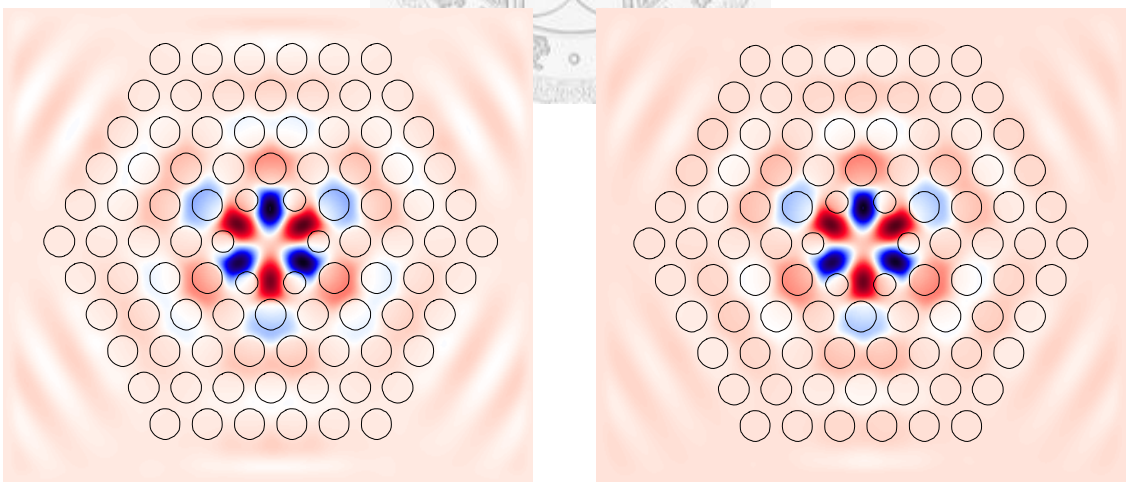

(c) $\theta = 30^\circ$, $\phi = 0^\circ$ (d) $\theta = 0^\circ$, $\phi = 0^\circ$

Figure 4.5 H_z-field profiles

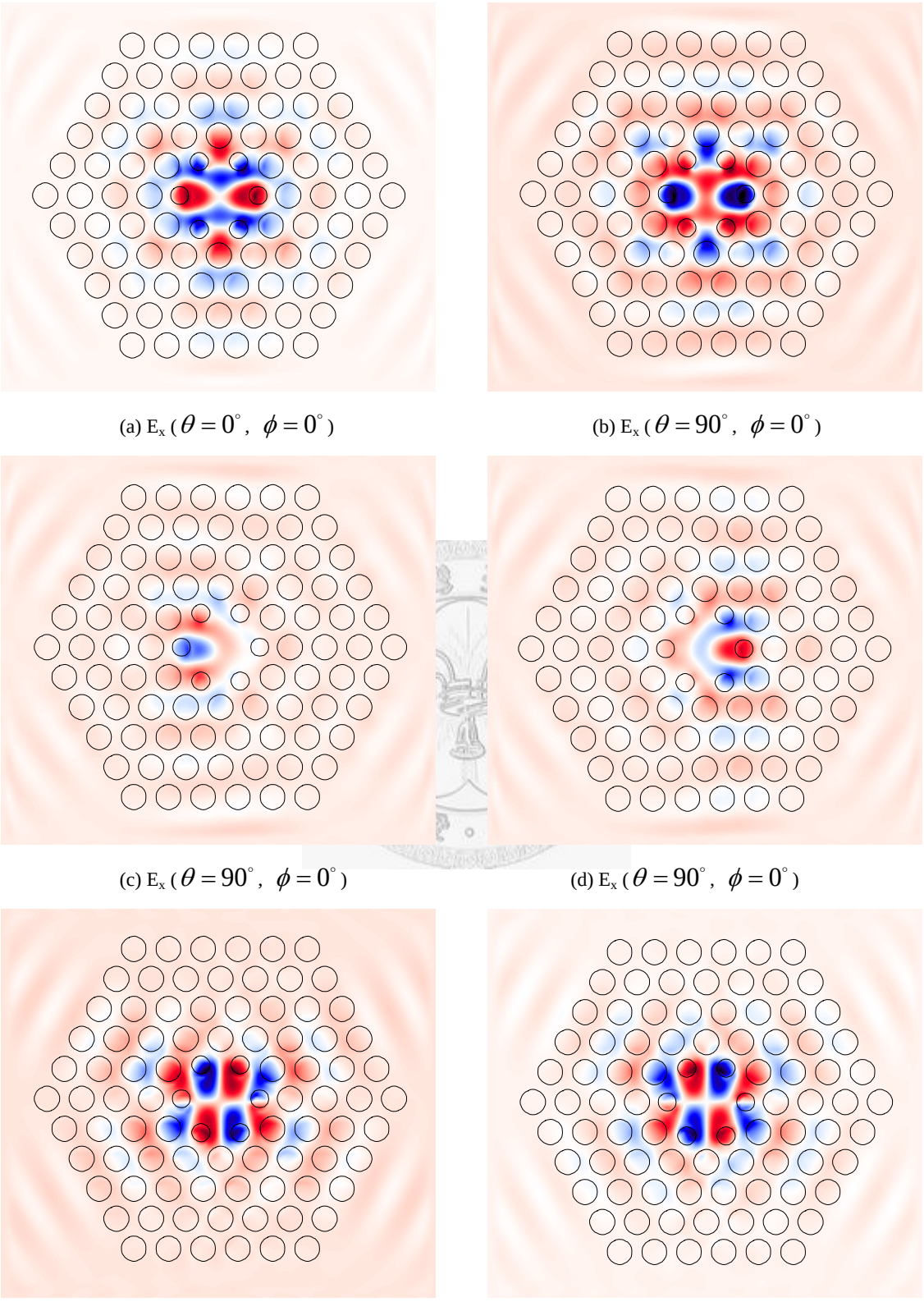

(a) E_x ($\theta = 0^\circ$, $\phi = 0^\circ$)

(b) E_x ($\theta = 90^\circ$, $\phi = 0^\circ$)

(c) E_x ($\theta = 90^\circ$, $\phi = 0^\circ$)

(d) E_x ($\theta = 90^\circ$, $\phi = 0^\circ$)

(e) E_y ($\theta = 90^\circ$, $\phi = 0^\circ$)

(f) E_y ($\theta = 0^\circ$, $\phi = 0^\circ$)

Figure 4.6 Transverse electric field profiles

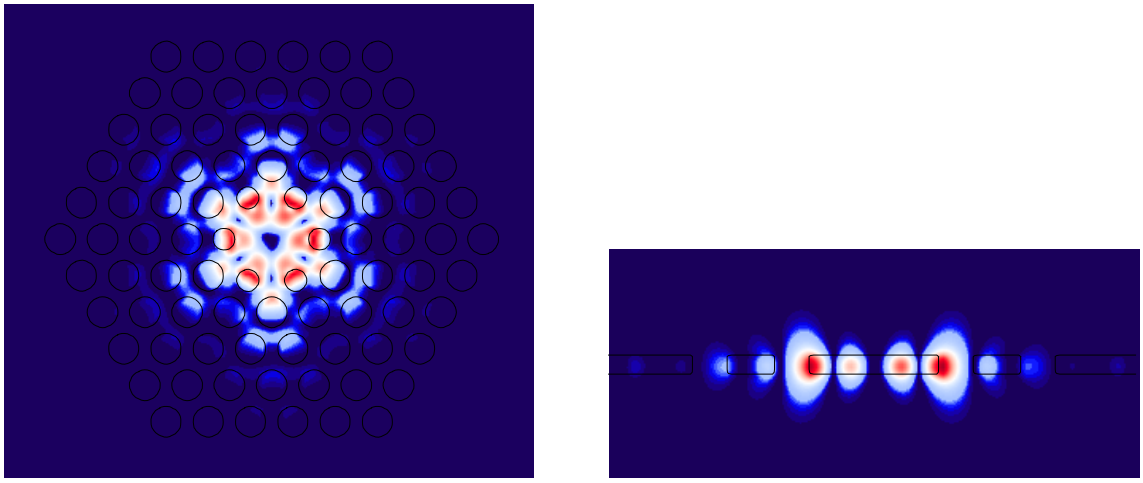

(a) Top view ($z = 0$) (b) Side view ($x = 0$)

Figure 4.7 Electric field intensity profiles of the hexapole mode ($\theta = 0^\circ$, $\phi = 0^\circ$)

This LC effect can also be confirmed by comparing with the FDTD simulation which can handle only non-birefringent materials (Figure 4.8). In this conventional FDTD simulation, the lasing mode at 1537 nm and 1558 nm can be found when n_{eff} is 1.4986 and 1.5833, respectively. $n_{eff} = 1.5833$ is the refractive index when the light propagating in-plane direction is mean angle $45°$-polarized with respect to the LC director. Thus, we can conclude that the conventional FDTD simulation well-predicts the lasing wavelength. However, It fails to predict the oscillation in the E_x-polarized light mode as shown Figure 4.6 (b)-(d). Here, we can also notice that there exists the quadrupole mode at $\lambda = 1545\ nm$ when $n_{eff} = 1.6841$, which actually doesn't occur.

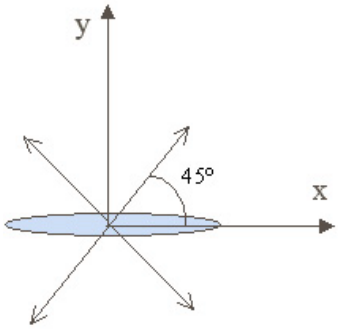

(a) Mean-polarized angle

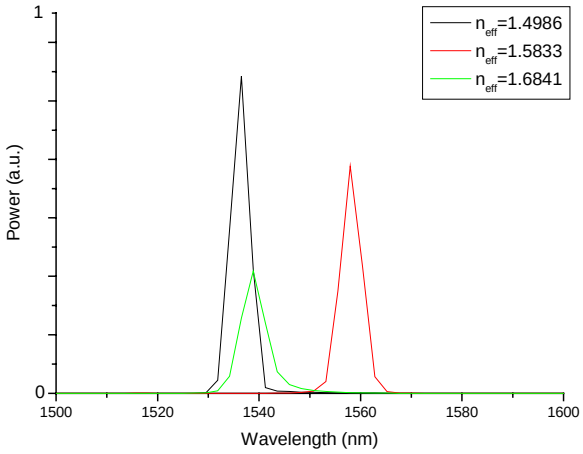

(b) Power spectrum (resolution limit : $2.5\ nm$)

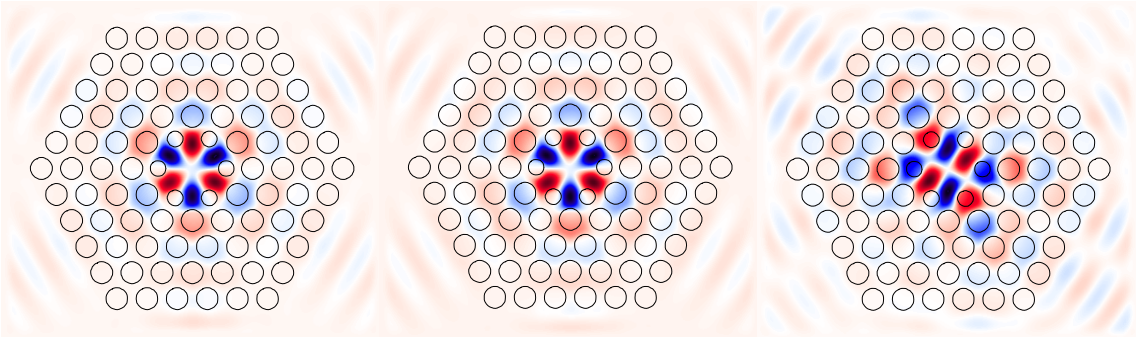

$n_{eff} = 1.4986$ $n_{eff} = 1.5833$ $n_{eff} = 1.6841$

(c) H_z field profiles

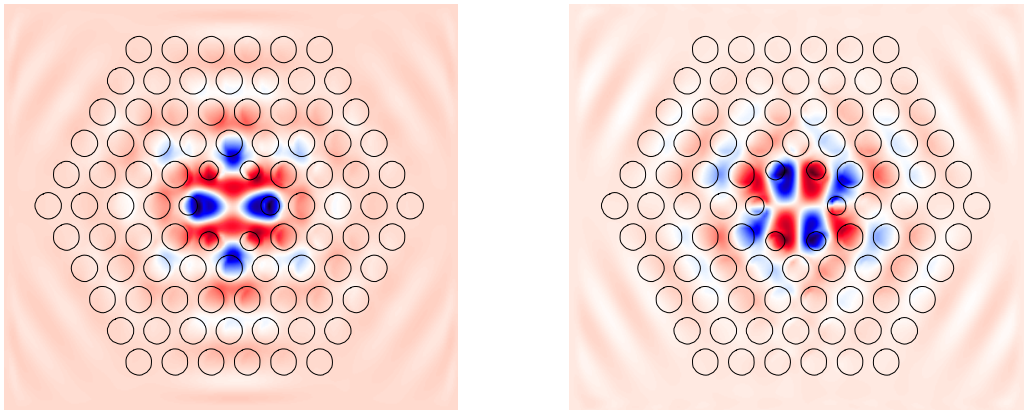

(d) E_x (left) and E_y (right) field profiles when $n_{eff} = 1.5833$

Figure 4.8 Conventional FDTD simulation results

4.2.2. Degeneracy Splitting (Design B)

From the Design B, we can get the dipole mode as shown in Figure 4.9. Since the dipole mode is doubly degerated, two degenerate modes are expected to appear in the ordinary air-hole 2D PhC slab structure [2]. However, if LCs are infiltrated into the air-holes and LC director is aligned parallel to x-axis ($\theta = 90^\circ$ $\phi = 0^\circ$) or y-axis ($\theta = 90^\circ$ $\phi = 90^\circ$), the degeneracy disappears as shown in Figure 4.9 (b)-(c). This is attributed to the symmetry breaking caused by LC alignment.

From Figure 4.10, we can notice that this is due to the partial polarization of in-plane electric fields. If we suitably design the defect, we expect that the intrinsic polarization of the lasing mode can be changed by LC alignment change. The electric field intensity profiles for each case are shown in Figure 4.11.

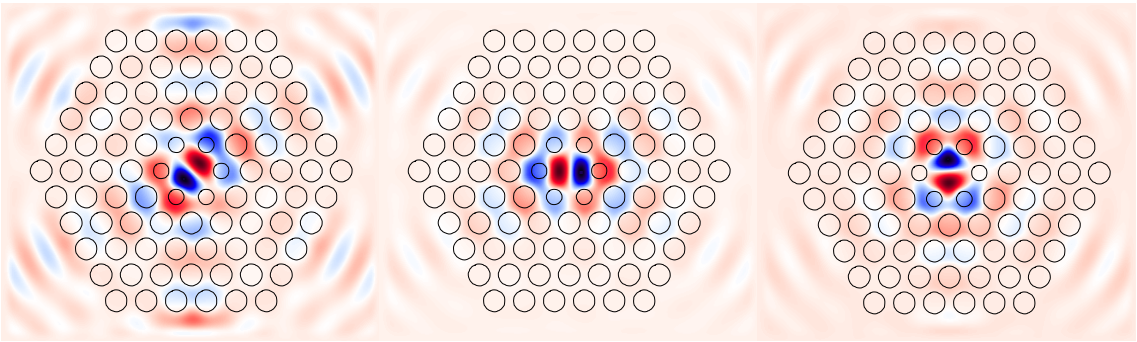

(a) $\theta = 0^\circ$, $\phi = 0^\circ$ (b) $\theta = 90^\circ$, $\phi = 0^\circ$ (c) $\theta = 90^\circ$, $\phi = 90^\circ$

Figure 4.9 H_z field profiles

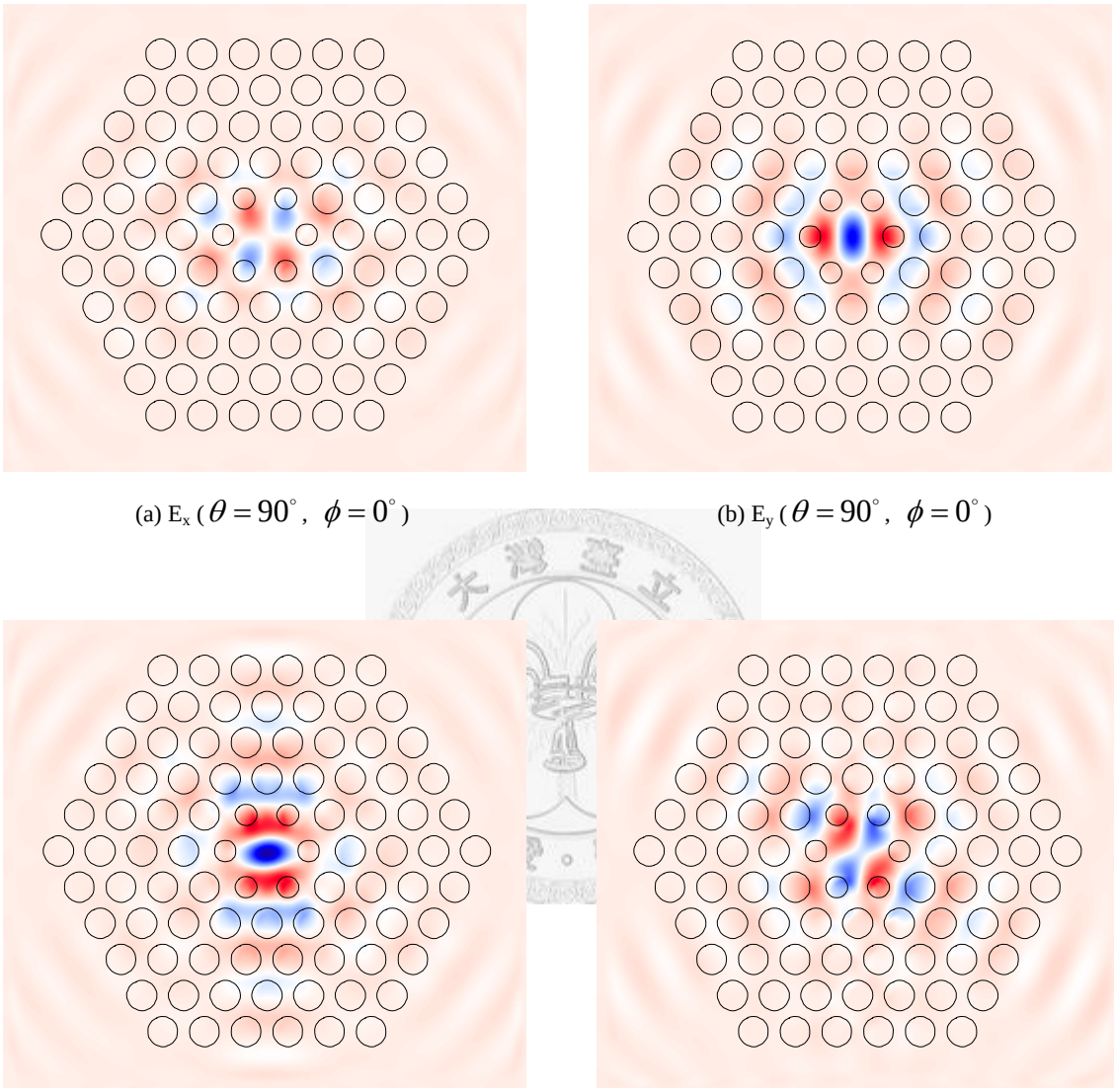

(a) E_x ($\theta = 90^\circ$, $\phi = 0^\circ$)

(b) E_y ($\theta = 90^\circ$, $\phi = 0^\circ$)

(c) E_x ($\theta = 90^\circ$, $\phi = 90^\circ$)

(d) E_y ($\theta = 90^\circ$, $\phi = 90^\circ$)

Figure 4.10 Transverse electric field profiles

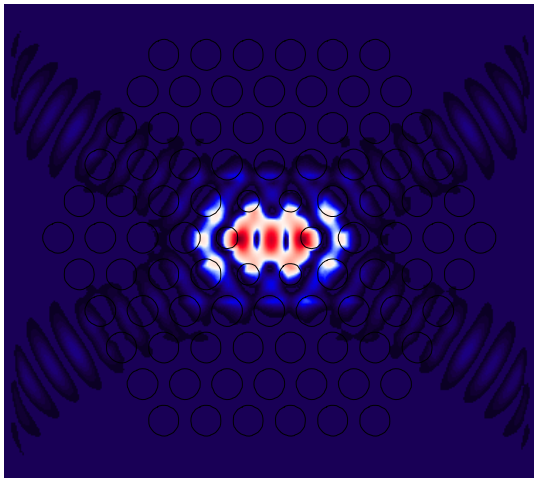

(a) Top view ($\theta = 90^\circ, \phi = 0^\circ$)

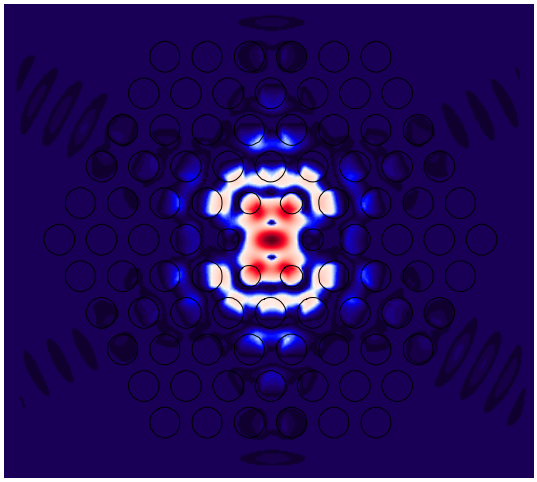

(b) Top view ($\theta = 90^\circ, \phi = 90^\circ$)

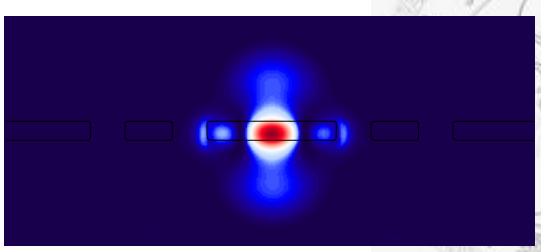

(c) Side view ($\theta = 90^\circ, \phi = 0^\circ, x = 0$)

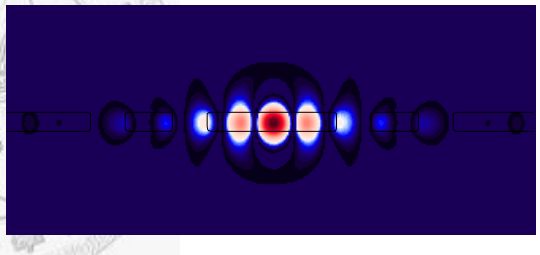

(d) Side view ($\theta = 90^\circ, \phi = 90^\circ, x = 0$)

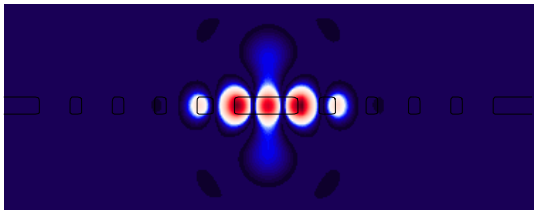

(e) Side view ($\theta = 90^\circ, \phi = 0^\circ, y = 0$)

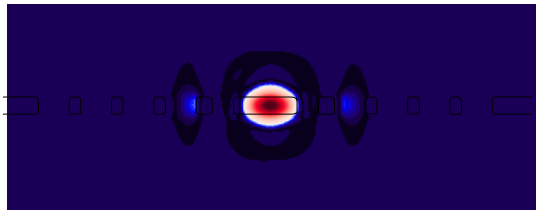

(f) Side view ($\theta = 90^\circ, \phi = 90^\circ, y = 0$)

Figure 4.11 Electric field intensity profiles

4.2.3. Lasing Mode Change (Design C)

In Figure 4.12, we can see the lasing wavelength shift. As θ changes from $90°$ to $60°$, the lasing wavelength shifts toward shorter wavelength region (from $1540\ nm$ to $1534\ nm$). When θ changes from $60°$ to $30°$, the lasing wavelength shifts toward longer wavelength region, which looks strange. However, when θ changes from $30°$ to $0°$, the lasing wavelength shifts from $1563\ nm$ to $1558\ nm$, again toward shorter wavelength region .

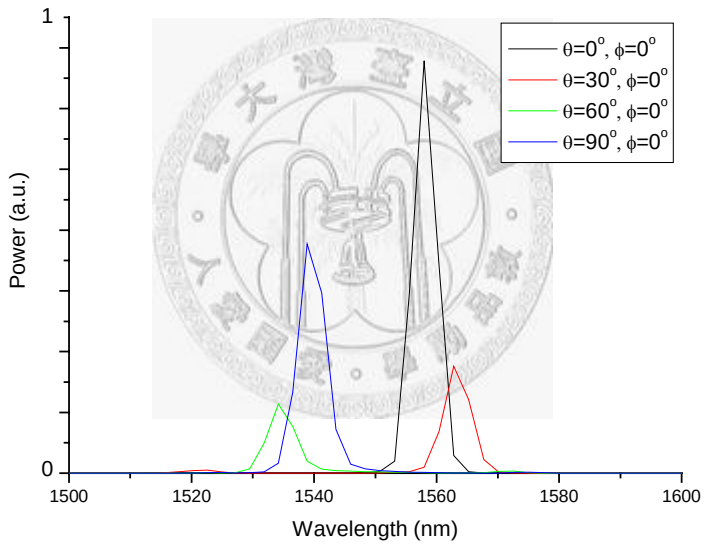

Figure 4.12 Power spectrum (resolution limit : $2.5\ nm$)

Here, we can guess, when θ changes from $60°$ to $30°$, the lasing mode is switched to another lasing mode. We can confirm it by analyzing the H_z field profiles at different θ.

From the Figure 4.13 (a) and (d), we can notice that the quadrupole mode of Q-factor 295 appears at $1540\ nm$ when $\theta = 90^\circ$ $\phi = 0^\circ$, and the hexapole mode of Q-factor

476 appears at 1558 *nm* when $\theta = 0^\circ$ $\phi = 0^\circ$

When $\theta = 60^\circ$, $\phi = 0^\circ$, the quadrupole mode appears at 1534 *nm*, yet the mode profile slightly deforms like Figure 4.13-(b). When $\theta = 30^\circ$, $\phi = 0^\circ$, the deformed hexapole mode is dominant (Figure 4.13-(c)). These deformed modes are probably attributed to the multiple mode mixing.

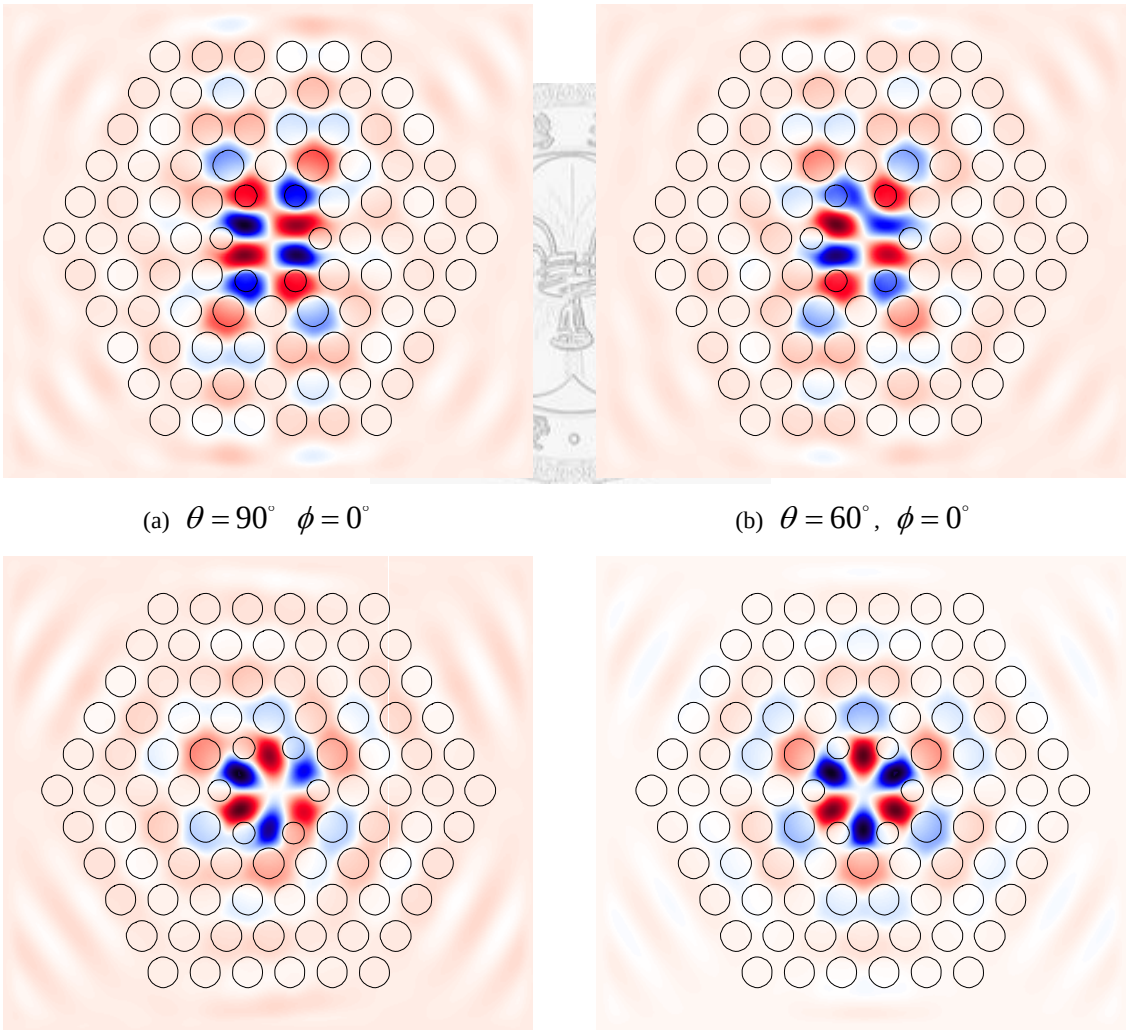

(a) $\theta = 90^\circ$ $\phi = 0^\circ$ (b) $\theta = 60^\circ$, $\phi = 0^\circ$

(c) $\theta = 30^\circ$, $\phi = 0^\circ$ (d) $\theta = 0^\circ$ $\phi = 0^\circ$

Figure 4.13 H_z field profiles

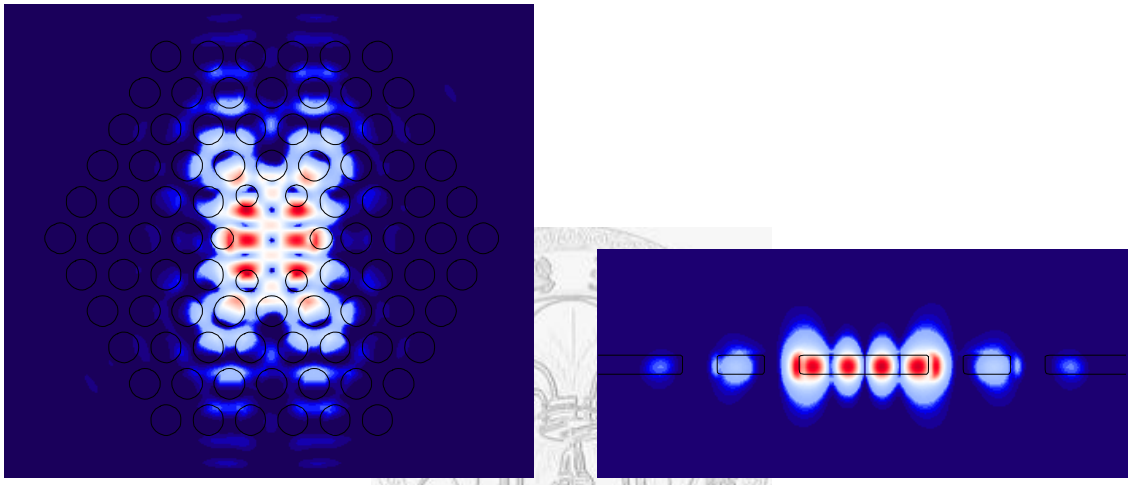

(a) Top view ($z = 0$) (b) Side view ($x = 0$)

Figure 4.14 Electric field intensity profiles of the quadrupole mode ($\theta = 90^\circ \quad \phi = 0^\circ$)

References

[1] B. Maune, M. Loncar, J. Witzens, M. Hochberg, T. Baehr-Jones, D. Psaltis, A. Scherer, and Y. Qiu, “Liquid crystal electric tuning of a photonic crystal laser,” Appl. Phys. Lett. 85, 360-362 (2004).

[2] Se-Heon Kim and Yong-Hee Lee, “Symmetry Relations of Two-Dimensional Photonic Crystal Cavity Modes”, IEEE JOURNAL OF QUANTUM ELECTRONICS, 39, 1081 (2003).

Chapter 5.

Conclusions

In this dissertation, we have developed the FDTD simulator which can handle the light propagation in LC medium, and have analyzed the characteristics of LC infiltrated tunable 2D PhC laser.

Merck E7, which is nematic LC at room temperature, is choosed as the suitable LC for its low refractive index and modest birefringence. Using Plane Wave Expansion (PWE) method, the 2D PhC slab is designed in consideration of the single mode condition, high Q-factor and the LC anchoring problem.

Only modified single-defect 2D PhC laser structures are considered due to the simplicity. Among the various defect designs, only three characteristic defect designs are discussed. In each defect design, the single mode lasing wavelength shift of ~20 nm (Design A), the degeneracy splitting (Design B), the lasing mode change (Design C) and the quality factor change are found as the arrangement of LCs changes. Moreover, the intrinsic laser polarization change by the LC alignment could be expected by suitable design.

With further refinement of our FDTD simulator, such as introducing Freedeticksz transition for the LC alignment, we hope that the method could be used to predict the characteristics of LC infiltrated tunable 2D PhC laser.